Journal of Materials Chemistry B

ROYAL SOCIETY OF CHEMISTRY

REVIEW

View Article Online
View Journal | View Issue

Cite this: J. Mater. Chem. B, 2024, 12, 6735

A nanoparticle-assisted signal-enhancement technique for lateral flow immunoassays

Fang Gao, [a] Shaonian Ye, [a] Lin Huang *[bc] and Zhengying Gu *[bc]

Received 21st April 2024,
Accepted 12th June 2024

DOI: 10.1039/d4tb00865k

rsc.li/materials-b

Lateral flow immunoassay (LFIA), an affordable and rapid paper-based detection technology, is employed extensively in clinical diagnosis, environmental monitoring, and food safety analysis. The COVID-19 pandemic underscored the validity and adoption of LFIA in performing large-scale clinical and public health testing. The unprecedented demand for prompt diagnostic responses and advances in nanotechnology have fueled the rise of next-generation LFIA technologies. The utilization of nanoparticles to amplify signals represents an innovative approach aimed at augmenting LFIA sensitivity. This review probes the nanoparticle-assisted amplification strategies in LFIA applications to secure low detection limits and expedited response rates. Emphasis is placed on comprehending the correlation between the physicochemical properties of nanoparticles and LFIA performance. Lastly, we shed light on the challenges and opportunities in this prolific field.

1. Introduction

The lateral flow immunoassay (LFIA) strip is a simple paper-based point-of-care (POC) testing device designed to rapidly and cost-effectively detect target analytes.[1] It fully aligns with the ASSURED criteria outlined by the World Health Organization for an ideal POC diagnostic device that is affordable, sensitive, specific, user-friendly, rapid and robust, equipment-free and deliverable.[2] Recently, the application of LFIA has expanded beyond clinical diagnostics[3–5] to include uses in food safety[6,7] and environmental monitoring.[8] The global market revenue for LFIAs is projected to increase from $20.5 billion in 2022 to an estimated $22.6 billion by 2027.[9] The COVID-19 pandemic has underscored the widespread applicability and effectiveness of LFIA testing for clinical and public health purposes.[10] However, the significant occurrence of false negatives has spurred the need for new generation LFIA technologies with a lower limit of detection (LoD).[11,12] Given the low concentration (10^{-16}–10^{-12} M) of crucial biomarkers in life-threatening diseases such as cancers and contagious diseases,[13,14]

[a] Institute of Energy Materials Science, University of Shanghai for Science and Technology, Shanghai 200093, P. R. China
[b] Department of Clinical Laboratory Medicine, Shanghai Chest Hospital, Shanghai Jiao Tong University School of Medicine, Shanghai, 200030, China. E-mail: guzhengying@shchest.org, linhuang@shsmu.edu.cn
[c] Shanghai Institute of Thoracic Oncology, Shanghai Chest Hospital, Shanghai Jiao Tong University School of Medicine, Shanghai, 200030, China

Fang Gao

Fang Gao earned her PhD from the University of Queensland, Australia, in 2022. She then worked as an Analytical Technical Officer at Sanitarium Health Food Company in Australia from 2022 to 2023. Since 2023, she has served as a Research Professor at the University of Shanghai for Science and Technology. Her primary research focuses on developing quantum dot-based biosensors and signal amplification systems for analytical chemistry, with applications in point-of-care diagnostics.

Shaonian Ye

Shaonian Ye received his BEng degree (2019) from Jingdezhen Ceramic University. He then joined Professor Fang Gao's group and is currently a Master's student at the University of Shanghai for Science and Technology. His major research focuses on the synthesis of quantum dot-based fluorescence biosensors and their application in point-of-care diagnosis.

achieving a lower LoD with LFIA is essential for effective interventions and therapies to help reduce mortality and morbidity.[15,16]

Significant efforts have been dedicated to improving detection sensitivity, as evidenced by numerous high-quality reviews in the field.[17–22] These endeavours encompass a range of strategies, including orientating antibodies on the labels and membranes,[23,24] exploring alternative recognition units such as aptamers[25,26] and glycans[27] *in lieu* of antibodies, integrating isothermal amplification methods[4] and/or clustered regularly interspaced short palindromic repeats (CRISPR) and CRISPR-associated (Cas) system[28–30] with LFIA, controlling the flow dynamics in LFIA,[31] developing dedicated reader devices,[32] and customizing labelling materials[10,33–35] like noble metal nanomaterials,[36–39] quantum dots (QDs),[40] upconversion nanomaterials,[41] and enzymes[42] to amplify colorimetric, surface-enhanced Raman scattering (SERS), fluorescence, chemiluminescence, and electrochemical[43] signals.

The utilization of nanoparticle-assisted signal amplification represents an innovative approach aimed at augmenting LFIA sensitivity. In this context, the term "nanoparticle" refers to a nanomaterial that serves to enhance the signal generated by the label material,[44] rather than functioning as the primary label material[45] for target analyte detection. For instance, while polystyrene spheres and silica nanoparticles are unable to independently generate a detectable signal, they boost the recognition process by enriching a large number of labels (*e.g.*, Eu(III) chelates and QDs).[46,47] Another illustration is provided by magnetic nanoparticles, which can effectively concentrate target analytes from complex samples and also carry a substantial quantity of labels for signal amplification to improve LFIA performance.[48] The physicochemical properties of nanoparticles, including size and surface chemistry, significantly impact the transport dynamics, reaction kinetics, and signal production that ultimately determine LFIA performance. However, there has been limited discourse on how to engineer nanoparticles to enhance their performance in LFIA applications.[22,40] Understanding the relationship between the physicochemical properties of a nanoparticle and its performance in LFIA signal amplification is crucial for advancing the development of LFIA with sub-picomolar LoD.[49] To date, there has been no comprehensive review of nanoparticle-assisted signal amplification strategies for LFIA, with a particular focus on the crucial involvement of nanoparticles.

Herein, we present a timely overview of the latest nanoparticle-assisted strategies for signal amplification in LFIA, aimed at achieving a lower LoD. The review is structured into three main sections: (1) utilizing nanoparticles to incorporate diverse labels (*e.g.*, small molecules, biomacromolecules, and nanomaterials) for multi-signal enhancement; (2) examining the impacts of key properties (size and surface chemistry) on their performance; and (3) discussing the challenges and prospects in applying tailored nanoparticles for the ultrasensitive LFIA. This review is intended to facilitate and enhance the evolution of the next generation of LFIA technology.

1.1. Nanoparticles for LFIA signal amplification

The LFIA, also known as the immunochromatographic assay, combines the principles of chromatography and immunochemical reactions.[50] As depicted in Scheme 1A, a typical LFIA strip consists of four key components: the sample pad, the conjugate pad, the reaction membrane, and the absorbent pad. The sample pad serves as the entry point for the sample, while the conjugate pad houses the labelled primary antibodies. The reaction membrane, usually made of nitrocellulose (NC), leverages the robust dipole interactions between the nitrate esters and the peptide bonds in the proteins to immobilize the primary and secondary antibodies.[51] This enables the formation of a test line and a control line based on the target antigen–antibody interaction. The absorbent pad functions as a waste reservoir, collecting the excess sample and reagents as they flow through the system.[52] The LFIA works *via* the capillary flow of the sample across the sequential pads, enabling rapid and user-friendly immunoassays on NC membranes. This integration of chromatographic separation and immunochemical reactions allows for the efficient detection and analysis of target analytes. Compared to other immunoassay techniques like enzyme-linked immunosorbent assay (ELISA), LFIA offers advantages such as simplicity, rapid analysis, portability, and

Lin Huang

Lin Huang received her PhD in biomedical engineering from Shanghai Jiao Tong University, China. Currently, she is a Senior Research Fellow (Principal Investigator) at Shanghai Chest Hospital, Shanghai Jiao Tong University School of Medicine, China. Her research interests focus on the development of novel materials for in vitro diagnostics based on various analytical methods.

Zhengying Gu

Zhengying Gu received her PhD in biomedical engineering from the University of Queensland, Australia. She is currently an Assistant Research Fellow at Shanghai Chest Hospital, Shanghai Jiao Tong University, School of Medicine, China. Her research interests focus on the study of immuno-metabolic interaction and the development of diagnostic and therapeutic nanotechnologies.

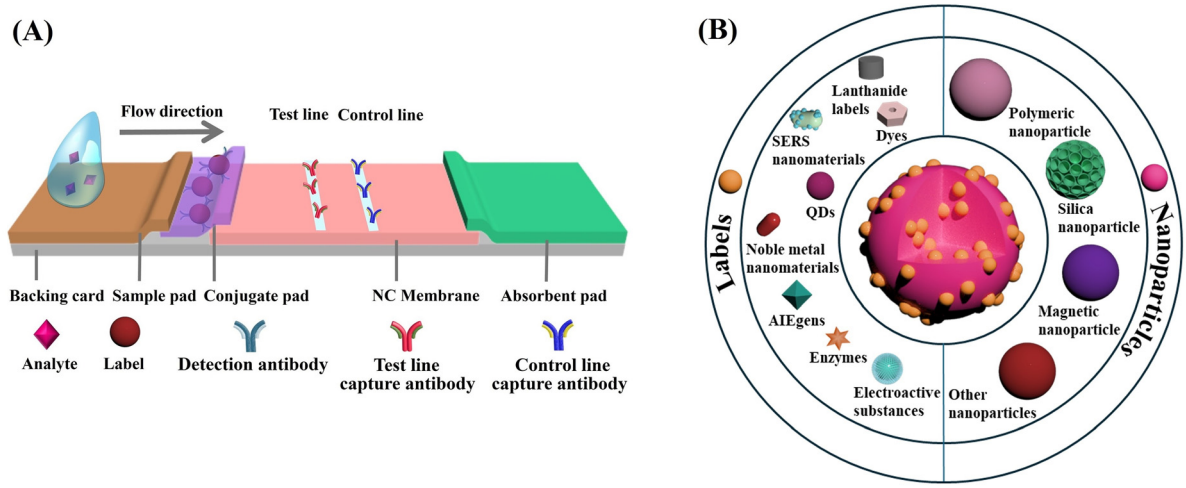

Scheme 1 Schematic diagram of (A) LFIA and (B) nanoparticles for LFIA signal amplification.

cost-effectiveness, making it a preferred choice for POC and on-site applications.[53]

Embedding sufficient labels onto a single nanoparticle is a highly effective strategy for improving the detection sensitivity of low abundance biomarkers. Much effort has been devoted to developing diverse nanoparticles for label enrichment and signal amplification, including polymeric nanoparticles, silica nanoparticles, magnetic nanoparticles, *etc.* (Scheme 1B).

1.1.1. Polymeric nanoparticles. Carboxyl-modified polystyrene nanospheres provide a useful platform for diagnostic applications.[54] They can be loaded with various fluorescent labels, such as dyes,[55] europium(III)–chelate,[56] AIEgens,[57] and QDs,[58] and can be conjugated with recognition molecules, such as antibodies and antigens.[59] The label materials can be enriched in polymeric nanoparticles through embedding into pre-synthesized nanoparticles, incorporating into an emulsion assembly, or *via* polymerization processes (Fig. 1).

1.1.1.1. Embedding into pre-synthesized nanoparticles. The swelling-coupled evaporation or centrifugation method is the most widely adopted approach for encapsulating labels such as dyes or QDs within polymeric nanoparticles. This method involves swelling polymer spheres in an organic solvent such as hexane,[58] chloroform,[60] dichloromethane,[61] or tetrahydrofuran.[57,59,62] After the labels permeate the interior of the spheres, the organic solvent is removed, causing the polymer network to contract and encapsulate the labels within particles. For example, Zhong *et al.* utilized hexane as the swelling solvent to prepare QD-embedded polystyrene nanobeads *via* this method.[58] The resulting nanobeads achieved a low LoD of 0.299 ng mL^{-1} for fetuin-B. The LoD of QD nanobead-based LFIA was 2.5 to 6.25 times lower than that of the colloidal Au-based LFIA in the detection of anticoagulant rodenticides.[60] Recently, the near-infrared emissive AIEgen-incorporated carboxyl-modified polystyrene nanospheres have been successfully fabricated through the swelling–centrifugation method and applied to LFIA (Fig. 2).[59] An estimated amount of 3.18×10^6 AIEgens was enriched in one polystyrene microsphere of 300 nm diameter, greatly amplifying the fluorescence signal of the obtained near-infrared label. The antibodies further modified on these polystyrene nanoparticles enable the detection of IgM and IgG against the severe acute respiratory syndrome coronavirus 2 (SARS-CoV-2) in clinical serum samples, with LoD values of 0.236 and 0.125 μg mL^{-1}, respectively. These values are comparable to those obtained by the ELISA, which yielded LoD values of 0.040 and 0.039 μg mL^{-1}. The near-infrared labelled-LFIA demonstrated a sensitivity of 78% for IgM detection and 95% for IgG detection as evaluated with 172 serum samples. The sensitivities are comparable to those observed in ELISA, which were found to

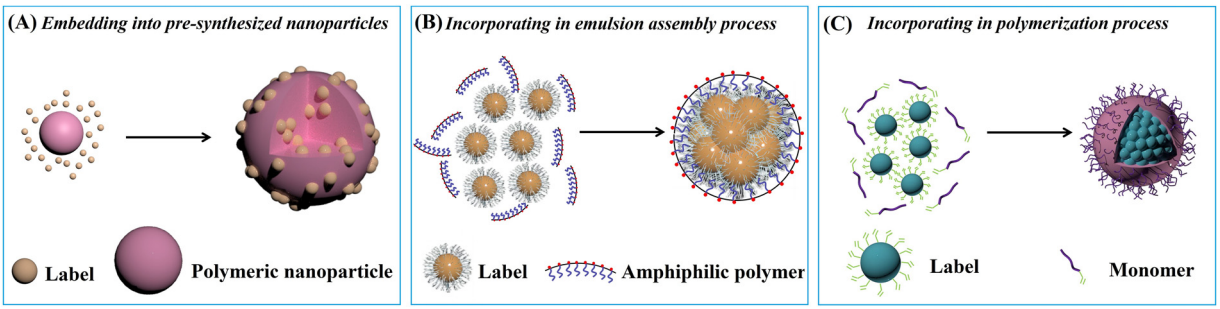

Fig. 1 Enrichment of label materials in polymeric nanoparticles through (A) embedding into pre-synthesized nanoparticles, (B) incorporating in emulsion assembly and (C) polymerization processes.

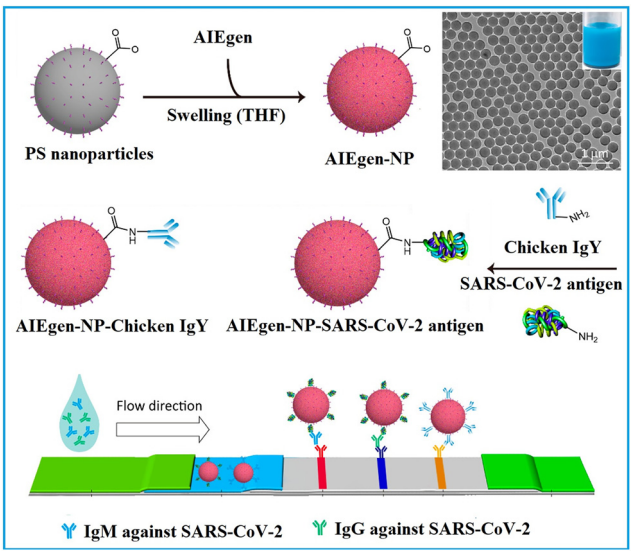

Fig. 2 The enrichment of labels to pre-synthesised polymeric nanoparticles. Reproduced with permission from ref. 59. Copyright 2021 American Chemical Society.

be 85 and 95% but superior to a commercial colloidal Au-based LFIA with a sensitivity of 41 and 85%. Owing to the significantly enhanced detection sensitivity of the near-infrared label-based LFIA, the test can detect the IgM or IgG antibodies in as early as one to seven days after the onset of symptoms, which is considerably earlier than the eight to fifteen days required by colloidal Au-based LFIA.

Besides the swelling-coupled evaporation or centrifugation method, the labels can be anchored on the surface of polymeric nanoparticles through electrostatic attraction,[63] or *in situ* growth.[64] For instance, the surface of commercial carboxyl-modified polystyrene nanospheres was rendered positively charged using poly(diallyldimethyl) ammonium chloride. These nanospheres were then incubated with an excess of negatively charged QDs under ultrasonication.[63] The resulting QD-decorated polystyrene nanospheres were coated with a silica shell to protect the fluorescence and for further bio-functionalization. The QD nanobeads were incorporated into a LFIA for SARS-CoV-2 antibody detection, resulting in more than a tenfold increase in detection sensitivity compared to the commercial assay based on colloidal Au. Matsumura *et al.* designed latex particles consisting of poly(2-vinylpyridine) cross-linked with divinylbenzene. Because of its positively charged pyridine moieties, metal ions ($AuCl_4^-$) can be adsorbed on their surface through electrostatic interactions. The Au labels were subsequently formed *in situ* by the reduction of adsorbed metal ions ($AuCl_4^-$).[65] The developed latex–Au nanocomposite contains multiple Au labels. Compared with conventional colloidal Au-labelled LFIA, the LoD of influenza A virus H1N1 antigen based on this nanocomposite-labelled LFIA was significantly lowered by 64 times.

1.1.1.2. Incorporating into an emulsion assembly process. Labels can be encapsulated into polymeric nanoparticles through emulsion strategy during the self-assembly of polymeric micelles. Typically, the hydrophobic label materials are initially dispersed in a nonpolar solvent (*e.g.* chloroform,[66–70] cyclohexane[71] and toluene[72]) containing amphiphilic poly(maleic anhydride-*alt*-1-octadecene) (PMAO) and/or hydrophobic poly(methyl methacrylate) (PMMA) to form the oil phase. The oil phase is subsequently combined with the aqueous phase containing surfactant and emulsified using an ultrasonic homogeniser to form the oil-in-water emulsion. Subsequently, the nonpolar solvent is evaporated to obtain the nanobeads. This approach has been used to fabricate nanobeads embedded with QDs,[66,69,73] gold nanomaterials[68,70,72] and AIEgens.[67,74]

Notably, the amphiphilic nature of PMAO allows for the co-assembly of functional building blocks with different solubility, resulting in a core–shell structure that spatially separates the building blocks. This separation is beneficial for maintaining the functionality of the building blocks and minimizing mutual interferences among them.[75–77] As exhibited in Fig. 3, hydrophobic Fe_3O_4 nanoparticles, AIEgens, and PMAO were dissolved in chloroform and then proceeded through micelle encapsulation in the aqueous phase, with SDS acting as the surfactant. The distinct solubility of Fe_3O_4 nanoparticles and AIEgens led to the formation of a core–shell nanostructure comprising a dense AIEgen core and a discretely packed Fe_3O_4 shell. The resultant AIEgen@Fe_3O_4 nanocomposite exhibits high fluorescence intensity attributed to enhanced photoluminescence from AIEgens stacking and reduced photon loss from the magnetic shell, as well as notable magnetic activity due to minimised magnetic shielding through magneto extraposition. With the assistance of magnetic operation, an LoD of 0.016 ng mL^{-1} was achieved by AIEgen@Fe_3O_4-based LFIA in the detection of lipoarabinomannan, representing a 44-fold higher sensitivity than colloidal Au-based LFIA.[77]

1.1.1.3. Incorporating into a polymerization process. The labels including europium(III)–chelate,[47,78,79] QDs,[80,81] dyes[82] and

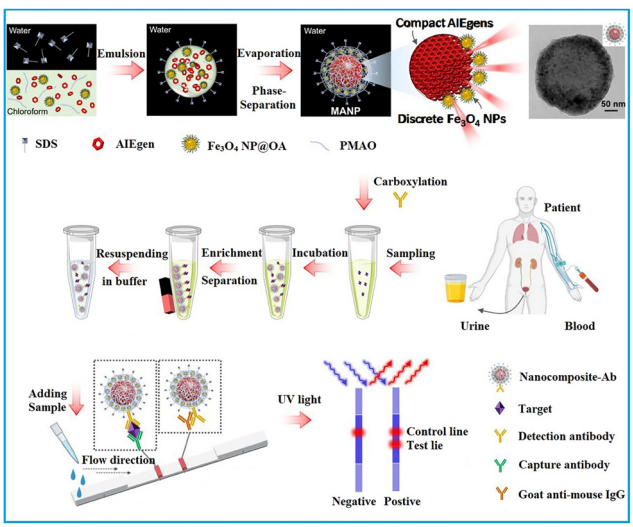

Fig. 3 The enrichment of labels in polymeric nanoparticles through mini-emulsion polymerisation. Reproduced with permission from ref. 77. Copyright 2021 Elsevier.

AIEgens[83] can also be embedded into polymeric nanoparticles through polymerization.[47,78–80,83] Typically, hydrophobic label materials are present in the oil phase, while carboxyl-providing monomers such as acrylic acid,[47] methacrylic acid,[80] methyl methacrylate,[82] and maleic anhydride[83] are present in the aqueous phase. Styrene monomers may be present in either the oil phase or aqueous phase with the aid of a surfactant, and all these components form a mini-emulsion. This emulsion then undergoes polymerization in the presence of an initiator (*e.g.* potassium persulfate,[80] azobisiobutyronitrile[83] and 4,4′-azobis(4-cyanovaleric acid)[78]) or under heat, resulting in the formation of polymeric nanospheres. As shown in Fig. 4, the carboxyl-modified Eu(III) chelate nanospheres were synthesised by using a one-step mini-emulsion polymerisation method.[78] The aqueous phase consisted of surfactant sodium dodecyl benzenesulfonate, carboxyl-providing acrylic acid and initiator 4,4′-azobis(4-cyanovaleric acid), which were mixed with styrene monomers, Eu(III) chelate labels and *n*-hexadecane in the oil phase. The mixture was emulsified under ultrasonication in an ice bath, followed by heating the mini-emulsion to 70 °C in an inlet atmosphere to allow polymerisation. During the one-step polymerisation, the Eu(III) chelates were immobilised within the interior hydrophobic environment and dispersed throughout the entire nanospheres. Compared with the swelling method, the Eu(III) chelate nanospheres prepared by the one-step polymerisation exhibited higher fluorescence intensity. The Eu(III) chelate nanosphere-based LFIAs demonstrated a LoD of 0.683 ng mL^{-1} in the detection of alpha-fetoprotein.[78]

This section illustrates three strategies for nanoparticle-based label enrichment. The swelling method is widely utilized for its operational simplicity and the consistent, reproducible sizes of the resulting nanobeads. Nevertheless, in this approach, labels tend to be predominantly located in the superficial layer of the polymeric nanoparticles, potentially restricting the loading capacity of labels. In contrast, nanobeads fabricated by the emulsion assembly and polymerization techniques may offer enhanced loading capacity. However, these strategies could pose challenges such as reduced reproducibility and label aggregation within the polymer frameworks.[84] The emulsion assembly strategy enables the concurrent assembly of diverse functional components with spatial separation. Nonetheless, nanobeads prepared using this approach often display non-uniform size distribution, potentially affecting assay reproducibility.[84,85]

1.1.2. Silica nanoparticles. Silica nanoparticles have been widely used for signal amplification in analytical applications,[86–88] although their specific applications in LFIA have been less discussed. Silica nanoparticles possess superior characteristics such as adjustable particle size and pore size, uniform particle size distribution, ease of functionalisation, and good stability, making them highly suitable for a wide range of applications in label accumulation and signal amplification.[89] Various types of silica nanoparticles, including nonporous silica nanoparticles, small-pored silica nanoparticles, and large-pored silica nanoparticles, have been extensively employed for signal amplification in LFIA platforms (Fig. 5).[90,91] These nanoparticles exhibit distinct features in terms of surface area, pore size, and pore structure, influencing their compatibility with different types of labels.

1.1.2.1. Nonporous silica nanoparticles. The nonporous silica nanoparticles can have labels enriched on their surface through physical or chemical adsorption.[92–97] A typical physical adsorption approach involves rendering silica nanoparticles positively charged by coating them with a cationic polyethyleneimine (PEI) layer[92,93] or functionalising them with amino groups,[94] which facilitate the adsorption of water-soluble negatively charged QDs[98,99] or gold nanomaterials.[94] Silica nanoparticles can be also functionalised with thiol groups to facilitate the assembly of hydrophobic QDs through thiol–metal coordination, which is a common chemical adsorption method used for label enrichment.[95–97] However, the loading capacity of surface enrichment is constrained by the limited surface area of nonporous silica nanoparticles.

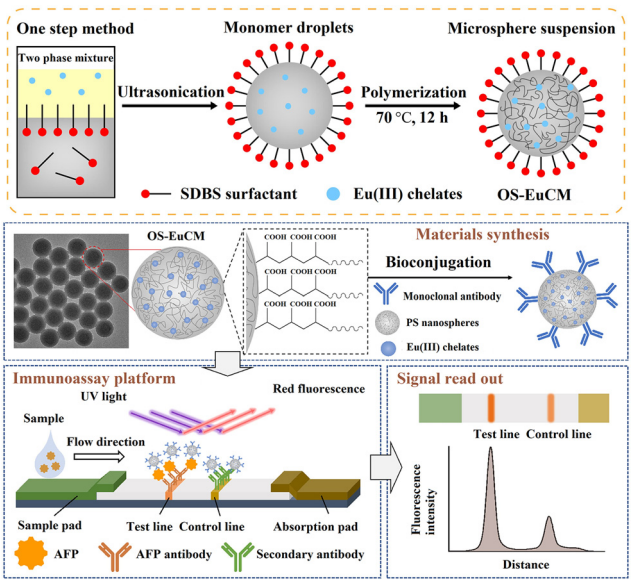

Fig. 4 The emulsion assembly strategy enabled spatial separation of different functional building blocks. Reproduced from ref. 78 with open access from John Wiley and Sons.

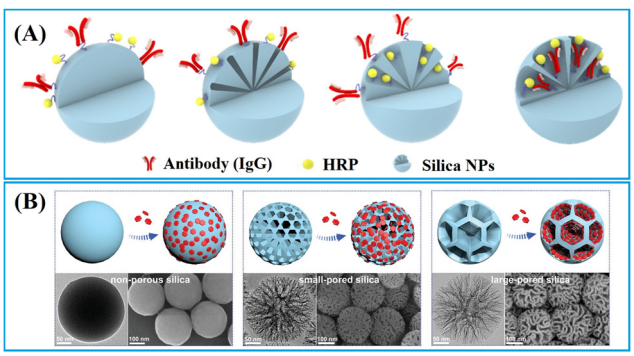

Fig. 5 Strategies for enriching (A) biomacromolecules and (B) nanomaterials to nonporous, small-pored, and large-pored silica nanoparticles. Reprinted with permission from ref. 90 and 91. Copyright 2021 American Chemical Society and 2024 John Wiley and Sons.

To enhance the loading capacity, a layer-by-layer assembly approach has been developed.[98–100] Through repetitive self-assembly of functional molecules and label adsorption, multi-shell labelled silica nanoparticles can be obtained. For example, the QD nanobeads with a triple-QD shell were obtained through a repeated PEI self-assembly followed by QD-adsorption.[99] The presence of numerous QDs not only significantly enhanced the fluorescence signal but also provide sufficient carboxyl groups for subsequent antibody conjugation. The QD nanobeads with enhanced fluorescence signal markedly lowered the LoD of LFIA in clinical diagnostics. The LoD of QD nanobead-based LFIA for detecting SARS-CoV-2 and influenza A virus H1N1 was found to be 5 pg mL^{-1} and 50 pfu mL^{-1}, respectively. Moreover, QD nanobead-based LFIA demonstrated exceptional accuracy and specificity when tested with throat swab samples. Its LoD was two orders of magnitude lower compared to the conventional colloidal Au-based LFIA.[99]

This layer-by-layer approach allows for facile co-assembly of various labels on the silica nanoparticles.[46,101,102] For instance, using this method, a multilayered nanocomposite composed of SiO_2–Au core and QD shell has been fabricated (Fig. 6A).[46] This composite material enables powerful colorimetric and fluorescent dual-signal output for rapid and sensitive *in situ* monkeypox virus antigen determination. The detection limits for the colorimetric and fluorometric modes were 0.5 and 0.0021 ng mL^{-1}, respectively. In the fluorometric mode, this method demonstrated a substantial enhancement in sensitivity for detecting the monkeypox virus, showing 238-fold and 3.3-fold improvements compared to the colloidal Au-based LFIA and ELISA methods, respectively.[46] Dou *et al.* prepared the dye-doped silica nanobeads with intensified fluorescence intensity through the PEI and poly(sodium-*p*-styrenesulfonate)-mediated layer-by-layer self-assembly approach,[103] The fluorescence signal of the resultant nanobeads (dyeing four times) was significantly enhanced compared to the once-dyed silica nanoparticles.[103] The dye-doped silica nanobead-based LFIA realised the quantitative detection of hemagglutinin antigen of H7N2 and H7N9 avian influenza viruses (AIVs), in the linear range of 0.1–10 ng mL^{-1} and LoD of 0.08 pg mL^{-1}.[103]

The noble metal nanomaterials, such as Au,[105–107] and Ag,[108] can be formed *in situ* on the surface of silica nanoparticles. Typically, the process begins with mixing the silica nanoparticles with solutions containing seeds[105–107] or ions[108] to form the seed/ion-decorated silica nanoparticles. The noble metal shell is then formed through the additional reduction of noble metal ions. For example, Au seeds are initially decorated on the surface of silica nanoparticles to facilitate the subsequent growth of the Au–shell.[107] During the Au–shell growth process, a growth solution is prepared, in which Au hydroxide is formed through the alkaline hydrolysis of chloroauric

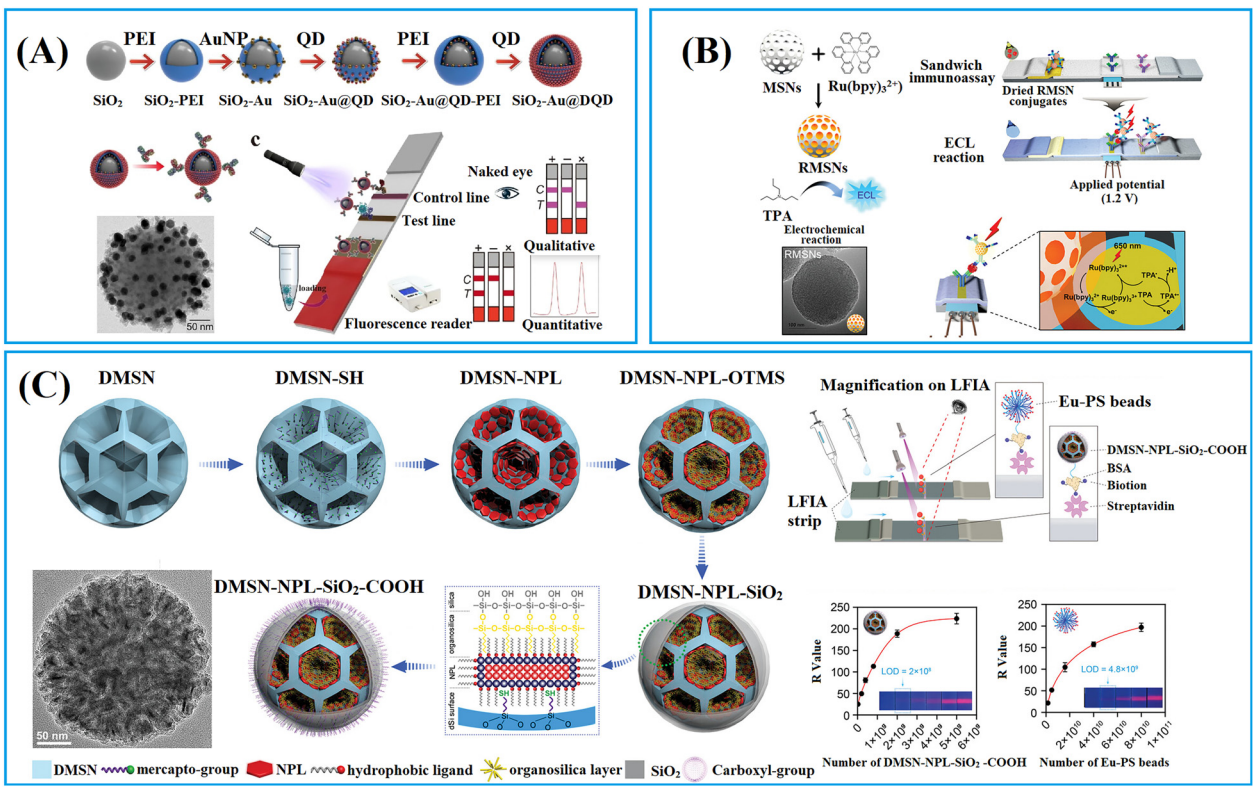

Fig. 6 Strategies for enriching labels to silica nanoparticles. (A) The enrichment of labels on the surface of nonporous silica nanospheres by a layer-by-layer assembly approach. Reproduced from ref. 46 with open access from Springer Nature. (B) The enrichment of small molecules in small-pored silica nanoparticles. Reproduced with permission from ref. 104. Copyright 2020 John Wiley and Sons. The enrichment (C) nanomaterials in large-pored silica nanoparticles. Reproduced with permission from ref. 91. Copyright 2024 John Wiley and Sons.

acid.[107] Subsequently, a suspension of Au seed-coated nanoparticles, a reducing agent such as hydroxylamine hydrochloride, and polyvinylpyrrolidone (PVP) are sequentially added to the growth solution, leading to the reduction of Au hydroxide ions $[Au(OH)_4]^-$ and the formation of Au shells.[107] The resulting silica nanoparticles, adorned with abundant Au labels, have exhibited a LoD of 0.5 ng mL^{-1} in the detection of heart-type fatty acid binding protein.[107]

1.1.2.2. Small-pored silica nanoparticles. Conventional mesoporous silica nanoparticles (MSNs) are a type of nanoparticles with pore size smaller than 10 nm,[109] suitable for enrichment and signal amplification of small molecular dyes such as tris(2,2′-bipyridyl)ruthenium(II) ($Ru(bpy)_3^{2+}$).[104] As illustrated in Fig. 6B, Hong *et al.* have developed an electrochemiluminescent LFIA for detection of cTnI at low concentrations using $Ru(bpy)_3^{2+}$-loaded MSNs as labels.[109] In comparison to non-porous silica, MSNs reduced the LoD by two orders of magnitude. This improvement is attributed to the porous structure of MSNs, facilitating a more effective loading of $Ru(bpy)_3^{2+}$, surpassing the loading capacity of non-porous silica by over 100 times. The $Ru(bpy)_3^{2+}$-loaded MSNs exhibited strong electrochemiluminescent signals in reaction to tripropylamine, generating an electrochemiluminescent image that can be captured by a CCD camera for quantification analysis. The electrochemiluminescent LFIA based on $Ru(bpy)_3^{2+}$-loaded MSNs enables the rapid detection of cTnI-spiked human serum within 20 min, achieving detection levels as low as 0.81 pg mL^{-1}.[109]

1.1.2.3. Large-pored silica nanoparticles. Innovative synthesis approaches have enabled the preparation of dendritic mesoporous silica nanoparticles (DMSNs) with a distinctive three-dimensional centre-radial pore structure, resulting in significant attention towards these DMSNs owing to their unique dendritic architecture.[110] The DMSNs exhibited large open pore channels and a highly accessible internal surface, distinguishing them as promising nanocarriers for biomacromolecules[90] and nanomaterials[91,111–113] when compared to conventional MSNs.

Jung *et al.* designed DMSNs with a pore size of 13 nm capable of size-selective immobilisation of antibodies (recognition molecules) and enzymes (labels).[90] The enzyme horseradish peroxidase (HRP) catalyses the oxidation of luminol using hydrogen peroxide to generate a product known as 3-aminophthalate, which can produce chemiluminescent signals emitting at a wavelength of 428 nm.[90] Given that the pore size (13 nm) of DMSNs is smaller than that of anti-AIV antibodies (10 nm × 15 nm) but larger than HRP (3.0 × 6.5 × 7.5 nm^3),[114] the anti-AIV antibodies were initially conjugated onto the outer surface of DMSNs to enhancing binding to AIV antigens. Subsequently, HRPs were loaded into the pores of DMSNs to amplify the chemiluminescence signals. It is noteworthy that, despite having higher loading capacity for HRP and anti-AIV antibodies, the DMSNs with larger pore size (19.2 nm) do not exhibit the lowest LoD due to the anchoring of anti-AIV antibodies within the inner pores. Therefore, the DMSNs with a 13 nm pore size were identified as the optimal nanoparticles. The chemiluminescent-LFIA using optimal DMSNs loaded with HRP and anti-AIV antibodies as labels for the nucleoprotein of the H3N2 AIV virus demonstrated a LoD of 5 pM. For avian influenza H9N2, H1N1 and H5N9 viruses, the LoD values were $10^{3.5}$, $10^{2.5}$, and 10^4 50% egg infective dose (EID_{50}) mL^{-1}, respectively. These values are 20 to 100 times lower compared to a commercial AIV rapid test kit.[90]

DMSNs have been proven to effectively enrich various nanomaterial-based labels, including QDs,[111,112,115,116] Au labels,[117] carbon dots,[113,118,119] and nanoplatelets.[91] For example, fluorescent silica nanospheres with controlled nanoplatelets incorporation have been developed to enhance the performance of LFIAs.[91] The synthesis method involved the controlled assembly of hydrophobic nanoplates into thiolated DMSNs through thiol–metal interaction, followed by the phase-transfer of the hydrophobic DMSN-nanoplate nanoassemblies through organosilica encapsulation and growth of the outer silica shell. The large open pore channels and highly accessible inner surface of DMSNs enabled the incorporation of flat/slit-shape nanoplatelets (24 nm in length, 11 nm in width and 4.4 nm in thickness) within DMSNs to amplify signal (Fig. 6C).[91] This unique structure has been shown to significantly enhance the fluorescence intensity, achieving a 246-fold and 4-fold increase in brightness compared to a standalone nanoplate and commercial europium-doped polystyrene, respectively.[91]

By employing a repeated coordination-driven assembly and phase-transfer process, various functional units, such as Fe_3O_4 nanoparticles, QDs and Au labels can be readily co-assembled into DMSNs.[120–123] Fig. 7A shows plasmonic–fluorescent silica nanocomposite composed of DMSNs loaded with Au labels and red-light emitting QDs using this method.[120] These nanocomposites were employed as the signal nanosphere in a CRISPR-based LFIA (Fig. 7B).[121] In negative detection mode, Cas12a enzyme remains inactive, resulting in the capture of all signal nanospheres by the test line. The inner colour filter effect of Au and red-light emitting QDs in the signal nanospheres cause a change in colour from green to red. Conversely, in the context of positive detection, the presence of target amplicons activates the Cas12a enzyme, triggering the collateral *trans*-cleavage of digoxin–ssDNA–biotin. In this scenario, only a few signal nanoparticles emitting red-light will be captured at the test line, remaining green. The cleavage activity of Cas12a and colorimetric readout capability, the assay can achieve a rapid visual detection limit of 1 copy μL^{-1} for *Salmonella typhimurium* genomic DNA within 1 h, surpassing the sensitivity of commercial colorimetric LFIAs.[121]

This section presents strategies for silica nanoparticles to enrich multiple labels for signal amplification. These labels can be adsorbed on the surface of the non-porous silica nanoparticles or embedded internally through layer-by-layer assembly and *in situ* synthesis. Selecting mesoporous nanoparticles with a matching pore structure based on the size of the label molecules or nanomaterials is another effective strategy to further enhance the concentration of label enrichment. Non-porous silica nanoparticles, known for their controllable particle size, excellent monodispersity and colloid stability, and

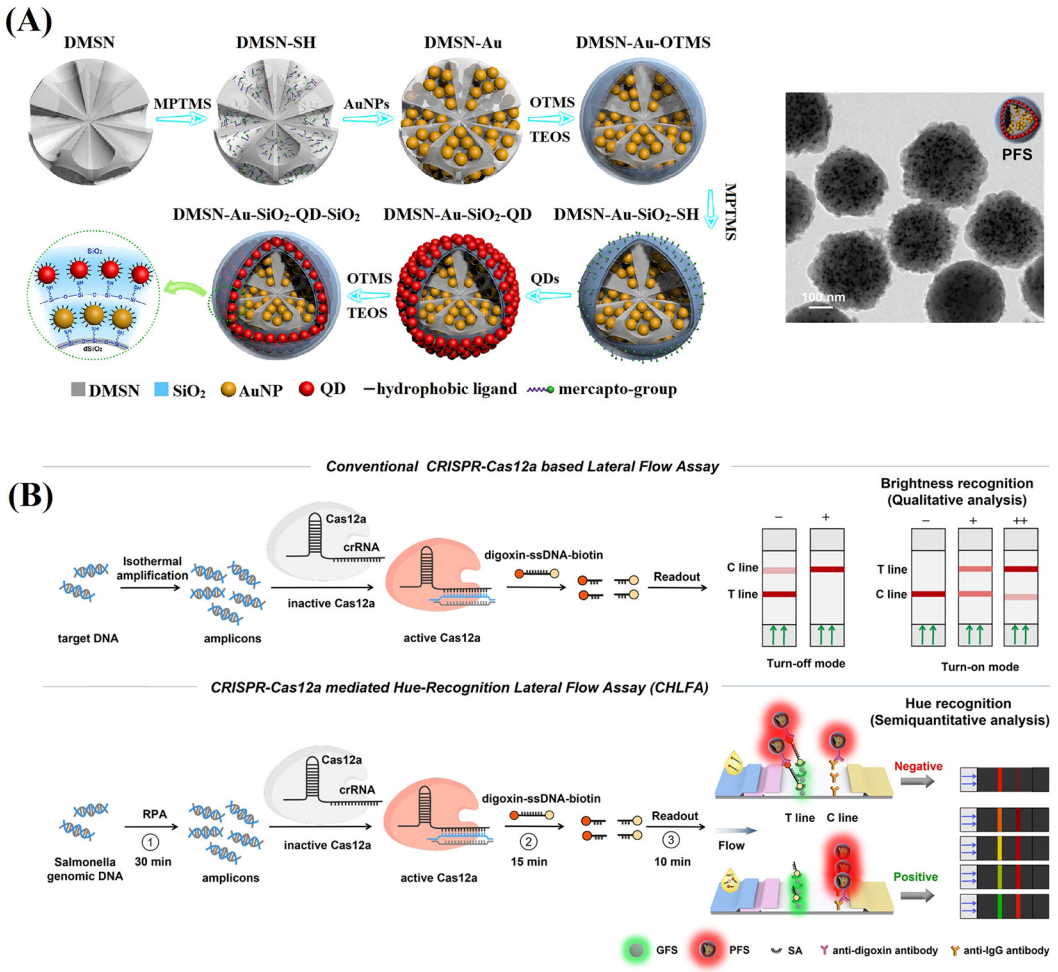

Fig. 7 Schematic representation of the enrichment of various functional units co-assembled into DMSNs through the repeated coordination-driven assembly and phase-transfer process. (A) The fabrication of plasmonic-fluorescent silica nanospheres by loading DMSNs with Au labels and QDs through the repetition of the coordination-driven assembly and phase-transfer process. Reproduced from ref. 120, Copyright 2020 American Chemical Society. (B) Implementation of plasmonic-fluorescent silica nanospheres as the signal nanosphere in a CRISPR-based LFIA. Reprinted from ref. 121, Copyright 2024 American Chemical Society.

ease of functionalisation, are widely used for label enrichment and LFIA signal amplification. Due to their limited surface area, non-porous silica nanoparticles have lower label loading capacity. In contrast, MSNs with a porous structure possess higher label loading capacity due to their larger surface area, significantly boosting the detection performance of LFIA. While conventional MSNs with pore size less than 10 nm are primarily used for the enrichment of small molecular labels, the DMSNs with a three-dimensional centre-radial pore structure excel in the enrichment of biomacromolecule and nanomaterial-based labels.

1.1.3. Magnetic nanoparticles. Magnetic nanoparticles (MNPs), such as Fe_3O_4 nanoparticles,[124–128] Fe_3O_4@silica nanoparticles,[129–132] Fe_3O_4@MOF nanoparticles,[48] and $MnFe_2O_4$ nanobeads,[133] exhibit superparamagnetic properties that enable the magnetic enrichment of target analytes in a complex matrix when subjected to an external magnetic field.[134] This feature streamlines LFIA operation following the magnetic enrichment of target analytes, thereby improving the detection performance significantly.[135]

A series of magnetic nanocomposite-based sensitive LFIA biosensors with amplified fluorescence, SERS, colorimetric and photothermal signals have been developed, such as the MNP@QD,[124,129,132,133,136] MNP@SERS,[125,128,137,138] MNP@nanozyme,[48,127,135,139] and MNP@Au.[140,141] Furthermore, Fe_3O_4 nanoparticles possess peroxidase-like properties and photothermal properties, offering advantages in enhancing the catalytic activity of Fe_3O_4@nanozyme[48,135] and the photothermal effect of Fe_3O_4@Au[140] respectively.

The PEI-mediated assembly approach is frequently utilized in the preparation of MNP@QD,[124,133,136,142] MNP@SERS,[125] and MNP@Au[141] nanocomposites. For example, Wang *et al.* developed a high-performance MNP@QD nanocomposite with a triple-QD shell to decrease the LoD of LFIA.[124] This nanocomposite consisted of an Fe_3O_4 core for magnetic separation and a triple-layer QD-shell containing numerous QDs for robust fluorescence signals. Upon conjugation with anti-SARS-CoV-2 spike antibodies/anti-nucleocapsid protein antibodies, the Fe_3O_4@QD was integrated into the LFIA system to detect

SARS-CoV-2 spike and nucleocapsid protein antigens. The Fe_3O_4@QD-based LFIA offers two detection modes. The direct mode enables rapid screening of suspected samples in a time frame of 10 minutes, while the enrichment mode allows for quantitative analysis of SARS-CoV-2 antigens at low concentrations without interference from the "hook effect". Owing to magnetic enrichment, the LoD for the two antigens in the enrichment mode was 0.5 pg mL^{-1} at a signal-to-noise ratio of 3, which is half as low as that in the direct mode.[124] As illustrated in Fig. 8, multilayered magnetic-core dual-shell nanocomposites with precisely controlled nanogaps were engineered using a PEI-mediated layer-by-layer assembly process.[125] The Fe_3O_4 core provided robust magnetic responsiveness, while the two layers Au@Ag satellites, separated by a 1 nm thick PEI interlayer, created narrow nanogaps and abundant hotspots. Furthermore, Raman reporters were integrated onto the surface of Au@Ag shells to enhance SERS signal. By modifying the nanocomposite with Raman reporter molecules and conjugating with four types of antibodies, the MNP@SERS nanocomposites could simultaneously detect four targets on two test lines with LoD reaching pg mL^{-1} levels. These detection limits were markedly lower than those of conventional Au-based LFIA and commercial ELISA kits, being at least 400 and 10 times lower, respectively.[125]

The *in situ* growth method has been used to prepare MNP@SERS,[128,137,138] MNP@nanozyme,[48,127,135,139] and MNP@Au[140] nanocomposites. For instance, Fe_3O_4@Pt nanocomposites[135] were synthesised by reducing chloroplatinic acid onto Fe_3O_4 nanoparticles using sodium citrate. The magnetic properties of Fe_3O_4 nanoparticles enabled magnetic enrichment in liquid samples, whereas the synergistic catalytic properties of Fe_3O_4 nanoparticles and Pt satellites allowed for colorimetric signal amplification through enzyme-like reactions. The integration of Fe_3O_4@Pt nanocomposites in LFIA strips led to a two-order-of-magnitude reduction in LoD compared to conventional LFIA based on colloidal Au.[135]

Increasing the loading density of Pt labels reduced the saturation magnetization of Fe_3O_4 nanocomposites owing to the intrinsic magnetic shielding effect of noble metal components.[48,128] In this context, an iron-based metal–organic framework (MOF) (MIL-100) with a thickness of 40 nm was utilized as a spacer layer to preserve the magnetism of Fe_3O_4 nanoparticles. The MIL-100 can accommodate Pt labels and improve the catalytic performance through the intrinsic peroxidase-like activity (Fig. 9).[48] The resultant Fe_3O_4@MOF@Pt nanocomposites achieved enhanced colorimetric signal brightness, rapid magnetic response, and ultrahigh peroxidase-mimicking activity, contributing to the enhancement of the sensitivity of LFIA. Integration of the nanocomposites with the dual-antibody sandwich LFIA platform enabled the detection of procalcitonin with remarkable sensitivity of 0.5 pg mL^{-1}. This level is approximately 2280 times greater

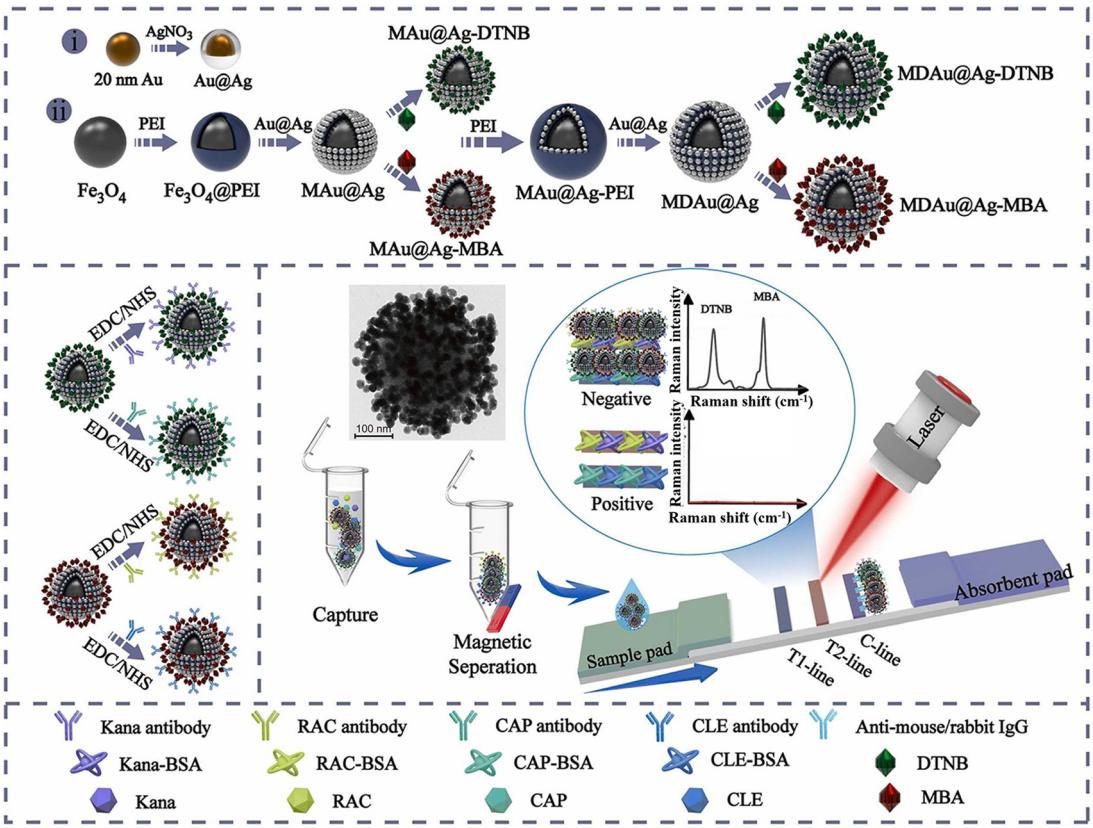

Fig. 8 The enrichment of labels on the surface of MNPs by a PEI-mediated assembly approach. Reproduced from ref. 125 with open access from Elsevier.

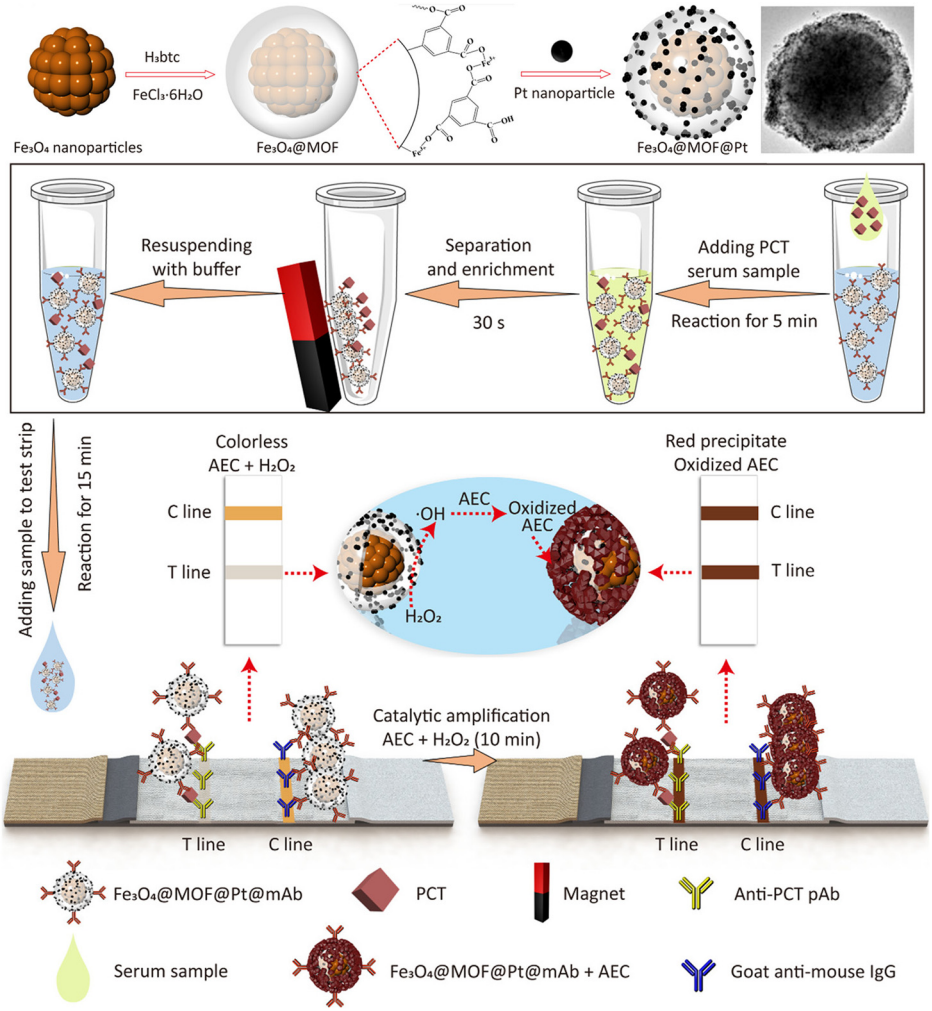

Fig. 9 The enrichment of labels on MNPs by an *in situ* growth method. Reproduced from ref. 48, Copyright 2022 American Chemical Society.

than that of conventional Au-based LFIAs and surpasses previously reported immunoassays.[48]

Enrichment of labels onto MNPs can be achieved through chemical adsorption.[129] Typically, the Fe_3O_4 nanoparticles are coated with a silica shell and amino functionalised using the Stöber method, followed by binding with carboxylated QDs using the EDC/NHS method.[129] A multifunctional nanocomposite was synthesized, consisting of an Fe_3O_4 core with diameter of 160 nm, a SiO_2 shell with thickness of 40 nm, and numerous small QD satellites.[129] Incorporating MNPs into QD-based LFIAs enhanced the precision and anti-interference capability in quantitative analysis, as target analytes can be rapidly enriched from complex samples under the influence of an external magnetic field. The LoD was determined to be 1.2×10^3 copy mL^{-1}, addressing the need for rapid and accurate adenovirus detection.[129]

In summary, the previously discussed MNP-label nanocomposites possess a core@shell structure, utilizing MNPs both as a magnetic separation tool and a stable nanocarrier for enriching diverse labels (*e.g.* QD, SERS labels, nanozyme, and Au labels). The assembly techniques predominantly employed for the preparation of MNP@QD and MNP@noble metals are the PEI-mediated assembly method and the *in situ* growth method. It is crucial to carefully select the reagent in the *in situ* growth method to ensure uniform plasmonic label coating. Compared to polymeric nanoparticles and silica nanoparticles, MNPs with intrinsic superparamagnetic properties enable direct operation of MNP-based LFIA after the magnetic enrichment of target analytes, which enhances the detection performance. It is essential to minimize the inherent magnetic shielding effect of noble metal components to preserve the saturation magnetization of Fe_3O_4 nanocomposites. Additionally, MNPs typically feature a nonporous structure, limiting label enrichment solely to the surface of the MNPs. In contrast, porous silica nanoparticles facilitate widespread label enrichment within their pores. Furthermore, polymeric nanoparticles can encapsulate numerous labels through the self-assembly of amphiphilic polymers in selective solvents, leading to a higher label loading capacity compared to MNPs without increasing particle size. While polymeric nanoparticles and silica nanoparticles boast exceptional optical clarity due to their amorphous nature, MNPs (particularly Fe_3O_4 nanoparticles) have a high

absorbance index. The high absorbance index causes MNPs to absorb the fluorescence signal of QDs and diminishes the signal intensity of the MNP@QD nanocomposite.

1.1.4. Other types of nanoparticles. In addition to polymeric nanoparticles, silica nanoparticles and MNPs, other types of nanoparticles including gold nanoparticles (AuNPs),[143–147] MOFs,[148–151] and carbon-based nanoparticles[152,153] have also been employed for both label enrichment and LFIA signal amplification.

1.1.4.1. AuNPs. AuNPs can serve as label materials for colorimetric assays and as a carrier for the enrichment of enzymes (*e.g.*, horseradish peroxidase (HRP),[154,155] polyHRP[143] and nanozyme[144]) and luminescent labels (*e.g.*, dyes[145–147] and bimetallic nanoclusters[156]) in chemiluminescent, fluorescent, colorimetric and electrochemiluminescent LFIAs. The immobilisation of polyHRP onto AuNPs led to a significant increase in HRP content per AuNP compared to HRP alone, approximately 15.7-fold higher.[143] The chemiluminescent signal generated by polyHRP-loaded AuNPs was 155-fold higher than that of HRP-loaded AuNPs. Integration of a time-programmable amplification step to the polyHRP-loaded AuNP-based LFIA platform enabled automation of the sequential enzyme/chemical reactions in the immunoassay and signal amplification. Using the developed LFIA platform, the LoD for cTnI was 0.84 pg mL^{-1}, representing a 595-fold improvement over colloidal Au-based LFIA.[143]

AuNPs exhibit distinct surface plasmon resonance properties that have garnered significant attention over the decades. The effect, known as the fluorescence enhancement, based on surface plasmon resonance, is currently employed in enhancing LIFA signals. Fig. 10 depicts a plasmonic fluor fabricated with a core of gold nanorod (GNR), a mesoporous silica ($mSiO_2$) shell, and a cyanine 5 (Cy5) fluorophore.[147] The choice of GNRs as the core was due to their two distinct surface plasmon resonances transverse and longitudinal, which culminate in a robust plasmonic resonance compared to gold nanospheres. Cy5 was selected for its high spectral overlap with GNRs. The 10.3 nm $mSiO_2$ shell not only encapsulates a considerable quantity of the Cy5 fluorescent material but also maintains an optimal distance between Cy5 and the GNRs. This step significantly amplified the fluorescence of Cy5 through plasmonic coupling between the GNRs and Cy5 in proximity, typically within 5–90 nm. The proposed plasmonic fluor LFIA facilitated sensitive detection of influenza A virus nucleocapsid protein with a remarkable LoD of 0.52 pg mL^{-1} within 20 min. Furthermore, it exhibited exceptional specificity and accuracy in analysing clinical samples for the influenza A virus.[147]

1.1.4.2. MOFs. MOFs, a class of crystalline porous material composed of metal ions and organic ligands, have characteristics, such as large surface areas, facile synthesis approaches, abundant functional groups, and chemical stability.[157] They have found extensive applications in biosensing,[157–159] catalysis,[160,161] and energy storage.[162] However, the use of MOFs for label enrichment and LFIA signal amplification is still at an early stage.[148–151,163,164] For example, the colorimetric catalytic nanocomposite in Fig. 11 utilized a multi-shell porous zeolitic imidazolate framework-8 (ZIF-8) to immobilize HRP, exhibiting commendable loading efficiency, catalytic activities, and signal luminosity.[148] This structure fostered more cavities for enzyme sequestration and facilitated an effective diffusion pathway for catalytic substrates. Further augmentation of the nanocomposite surface with a polydopamine (PDA) layer amplified the signal brightness and proffered a flexible tethering site for HRP immobilization, thereby escalating the enzyme quantity efficiently. This ZIF-based LFIA platform achieved an ultrasensitive assay for cTnI with a post-catalytic naked-eye colorimetric detection limit of an impressive 0.01 ng mL^{-1},

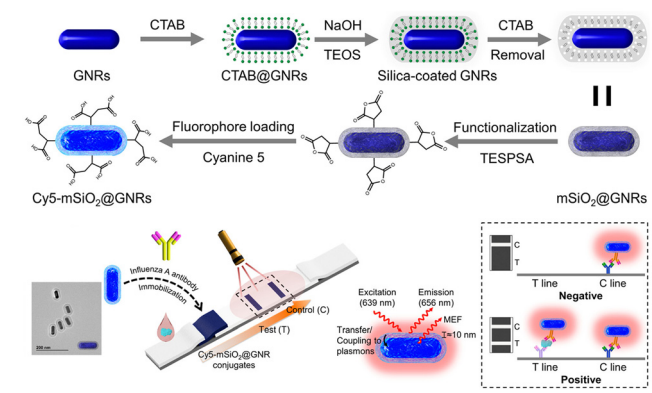

Fig. 10 The use of AuNPs for labels enrichment and LFIA signal amplification. Reproduced with permission from ref. 147. Copyright 2023 American Chemical Society.

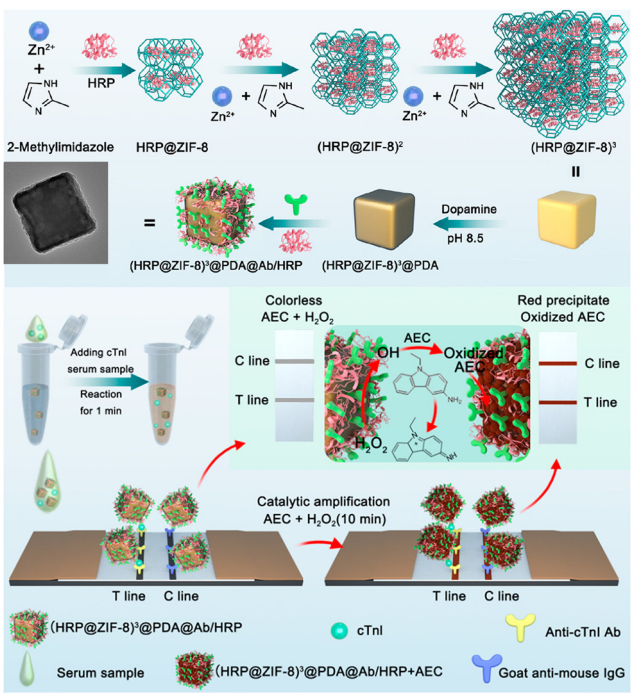

Fig. 11 The use of MOF for labels enrichment and LFIA signal amplification. Reproduced with permission from ref. 148. Copyright 2023 American Chemical Society.

which was 100-fold higher than its counterpart Au@PDA-based LFIA.[148] Zirconium-based MOFs have been reported to facilitate the *in situ* growth of the MOF–Au nanocomposite.[164] Compared to the traditional colloidal Au-based LFIA, the LoD of MOF–Au-labelled LFIA for human chorionic gonadotropin was reduced by 10.6 times.

1.1.4.3. Carbon nanomaterials. Carbon nanomaterials, known for their distinct properties, such as excellent chemical stability, large surface area and cost-effective synthesis, are ideal nanoparticles for label enrichment.[152,153,165] Among these, the graphite-like g-C_3N_4 nanosheets with large surface areas have been applied to enrich abundant Au nanomaterials on their surface to amplify signals and improve the performance of g-C_3N_4–Au-based LFIA.[153] The LoD of g-C_3N_4–Au-based LFIA for 17β-estradiol in foods was 0.5 ng mL^{-1}, exhibiting a three-fold enhancement in analytical sensitivity compared to colloidal Au-based LFIA.[153] A three-dimensional membrane-like SERS nanocomposite based on graphene oxide (GO) has been incorporated into LFIA for the sensitive detection of various pathogens.[152] The process, as illustrated in Fig. 12, initiates by coating the GO sheet with a positively charged PEI layer to attract small Au seeds (3 nm). Subsequently, the Au shell was coated on the surface of the GO@Au seed nanosheet using hydroxylamine hydrochloride to reduce chloroauric acid. Then, a 0.5 nm PEI layer was applied to the synthesized GO@Au surface to act as an interlayer. This interlayer was instrumental in creating a precise nanogap to load Raman dye molecules and Ag satellites *via* electrostatic interaction. The process generated numerous SERS hotspots and offered a multitude of surface sites for bacterial adhesion. By integrating two different Raman reporter molecules with non-intersecting Raman peaks into GO@Au@Ag, and conjugating them with four antibodies, the biosensor facilitates the concurrent identification of four pathogens at dual test lines. The GO@Au@Ag nanostickers are highly effective at adhering to the bacteria surface, yielding stronger SERS signals and aiding in the mobility of bacterial nanocomplexes. This, in turn, leads to an improvement in the sensitivity of LFIA for bacteria detection. This biosensor can accurately quantify four distinct types of bacteria in actual clinical samples, achieving a minimal detection limit of 9 cells mL^{-1}.[152]

Table 1 summarises the advantages and limitations of different nanoparticles applied in LIFA signal amplification. Au nanomaterials have been extensively studied not only as labels of LFIA but also as nanocarriers for label enrichment and LFIA signal amplification due to their ease of preparation and conjugation, mass production capacity, and uniform particle size. Smaller AuNPs (<50 nm) exhibit reduced non-specific binding compared to other types of nanoparticles, although they have a lower loading capacity (~10 times less) for labels. These smaller AuNPs also offer faster migration speed, allowing for a 15-minute one-step assay, considerably quicker than 50-minute two-step assay required for larger silica nanoparticles (200 nm). The plasmonic properties of AuNPs enable them to boost the fluorescence of fluorophores. MOFs with high surface areas and abundant functional groups are suitable for label enrichment, but their water instability poses a significant challenge when applied to LFIA signal amplification for detecting target analytes in serum or urine samples. Two-dimensional carbon nanomaterials with expansive surface areas and cost-effectiveness are promising for label enrichment, however their nonuniform size distribution may impair the reproducibility of the assays.

1.2. Engineering nanoparticles for LFIA signal amplification

LFIA integrates the physical, chemical, and optical properties of label materials, with their transport dynamics, reaction kinetics and signal generation all playing significant roles in

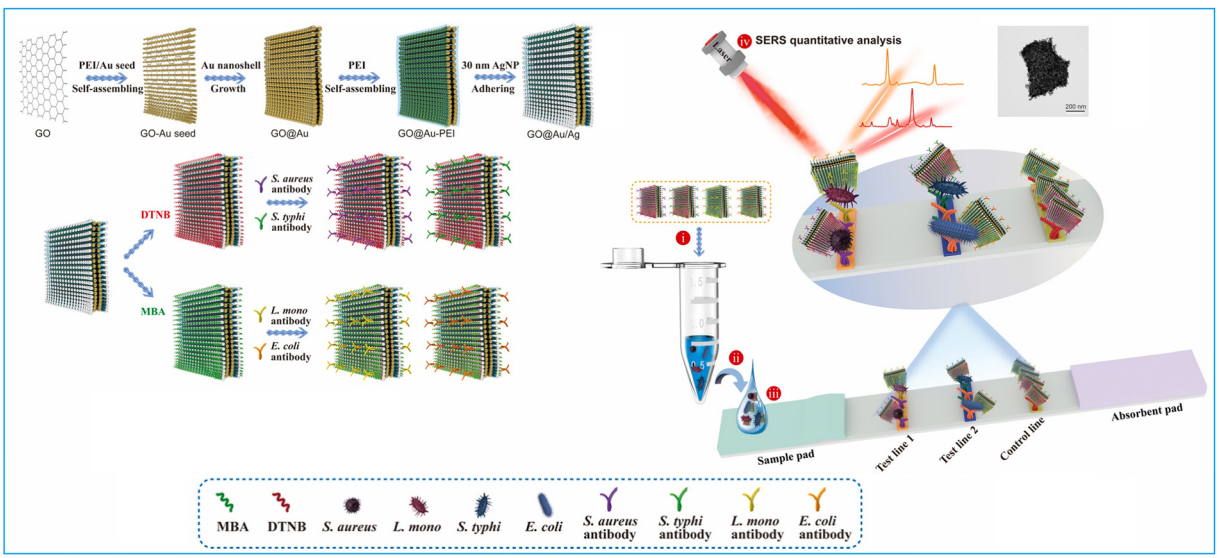

Fig. 12 The use of graphene oxide nanosheets for labels enrichment and LFIA signal amplification. Reproduced with permission from ref. 152. Copyright 2022 Elsevier.

Table 1 Summary of advantages and limitations of different nanoparticles

Nanoparticles		Advantages		Limitations		Ref.
Polymer nanoparticles	Embedding into pre-synthesized nanoparticles	Excellent optical clarity	Very easy operation, uniform size distribution and good reproducibility	Label distribution inhomogeneity problem	Limited label loading capacity of nano-sized labels	59
	Incorporating in an emulsion assembly process		Easy operation, high label loading capacity and relatively controllable assembly process		Nonuniform size distribution, and low reproducibility	77
	Incorporating in the polymerization process		Medium label loading capacity and uniform size distribution		Carefully controlled operation condition	78 and 80
Silica nanoparticles	Nonporous	Excellent optical clarity, ease-of-functionalisation, very controllable assembly process	Excellent colloidal stability	Tedious operation process	Limited label loading capacity	46
	Small-pored		Suitable for molecular-sized labels		Not very suitable for nano-sized labels	109
	Large-pored		Very high label loading capacity			91
MNPs		Magnetic enrichment of target analytes, catalytic and photothermal properties		Tedious operation process, limited label loading capacity and high absorbance index		129 and 140
AuNPs		Ease-of-preparation and conjugation, mass production capacity, uniform particle size, less non-specific binding, catalytic and plasmonic properties		Limited label loading capacity and high absorbance index		144 and 147
MOFs		High label loading capacity and ease-of-functionalisation		Water instability		**148**
Carbon nanomaterials		High label loading capacity and low cost		Nonuniform size distribution		152

determining their performance within LFIA applications. The previous section demonstrated that the enrichment of labels on a single nanocarrier to form nanoparticle-label composites is an effective strategy for enhancing signal intensity. However, the size and surface chemical properties of these composite nano-labelling materials greatly influence the transport dynamics, reaction kinetics, and signal generation in LFIA. For example, particle size simultaneously impacts the label loading capacity (signal generation) and diffusion rate (transport dynamics).[166] Moreover, surface chemistry greatly affects its water dispersibility (transport dynamics), antibody-antigen interaction (reaction kinetics) and label signal intensity (signal generation).[66,115,167] The impact of size and surface chemistry of nanoparticle/resultant nanocomposite on the LFIA performance is complex. Therefore, a thorough comprehension of the relationship between the physicochemical properties of nanoparticles and their performance in LFIA signal amplification would facilitate the rational design of nanoparticle-label composites applied in LFIA. This section will delve into the impact of nanoparticle size and surface chemistry on their performance in LFIA applications.

1.2.1. Size-controlled signal amplification strategies in LFIA. The size of a nanoparticle-label nanocomposite is a pivotal factor determining its performance in LFIA, impacting the signal generation, transport dynamics, and reaction kinetics of the nanocomposite in LFIA.[72,83,116,166,168] Increasing the particle size enhances the loading capacity and binding affinity of nanocomposites due to a larger surface area, allowing for more labels and antibodies to be accommodated. However, based on the Stokes–Einstein equation, larger nanoparticles exhibited decreased diffusion rates, resulting in fewer nanoparticles binding to the antibodies immobilised on the NC pore walls. Therefore, achieving optimal performance in LFIA requires a delicate balance between signal strength and diffusion dynamics.

1.2.1.1. The impact on signal intensity. The signal intensity of a nanoparticle-label nanocomposite typically correlates positively with its particle size, due to the increased surface area of individual nanoparticles, enhancing their capacity for label loading. For example, the colorimetric and fluorescence signals of nanobeads loaded with Au labels,[68,70,72] QDs,[116,166] and AIEgens[83] enhance significantly as their particle size increases. In Fig. 13A, the optical density of Au-embedded nanobeads increases by over 10-fold as the size grows from 100 to 400 nm.[72] These Au-embedded nanobeads were prepared using an emulsion assembly strategy.[72] Within the emulsion system (oil-in-water), adjustment of surfactant concentration, oil-to-water ratio, and ultrasonic power enables facile control of particle size. Generally, an increase in surfactant concentration or oil-to-water ratio leads to particle size reduction, while higher ultrasonic power results in size increase.[72] Similarly, the fluorescence intensity of AIEgen-embedded polymeric nanobeads escalates as their size expands.[83] This mechanism also applies to nanoparticle-label composites using large-pore nanoparticles as a carrier. As shown in Fig. 13B, the fluorescence intensity of the DMSN-QD nanocomposite amplifies by over 30-fold as the DMSN size increases from 138 to 471 nm.[116] Monodispersed DMSNs were synthesized using an anion-assisted approach[169] with sodium salicylate as the structure-directing agent. Control over the size of DMSNs can be easily achieved by adjusting the amount of sodium salicylate and ethanol,[116] improving the surface area of individual particles and label loading capacity.

1.2.1.2. The impact on binding quantity. Since LFIA comprises a chromatographic system and immunochemical reactions, the

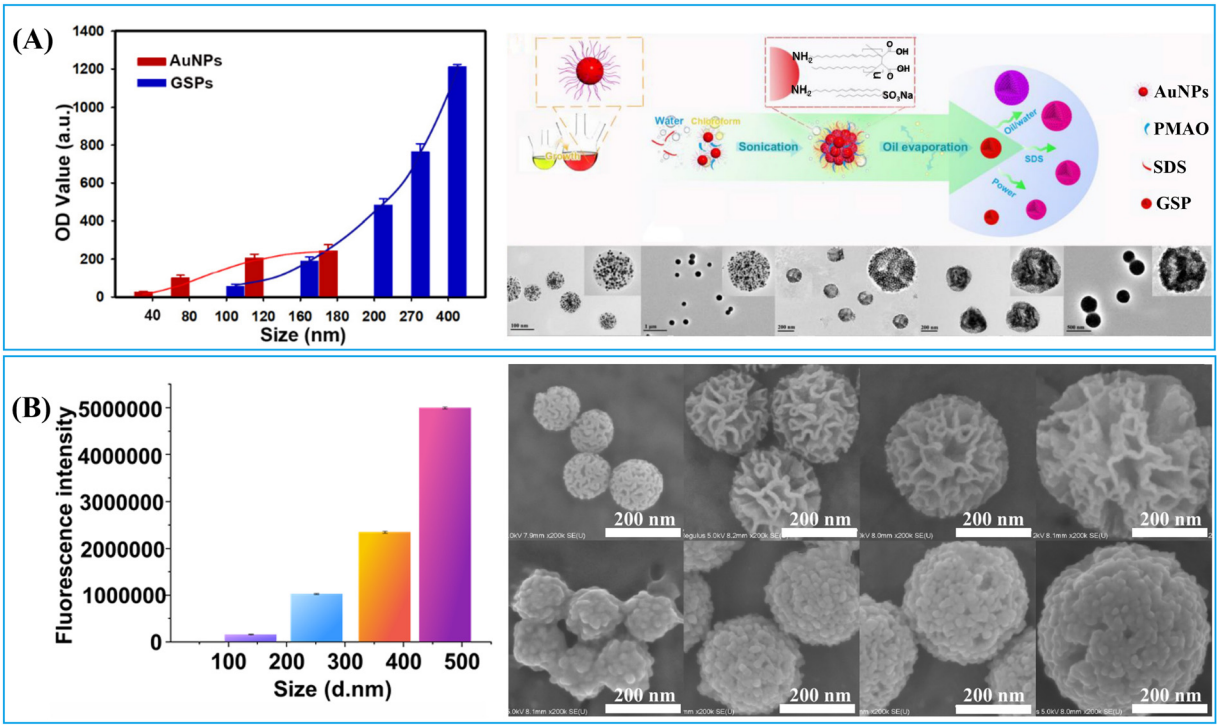

Fig. 13 The impact of particle size on its signal generation and size-controlled synthesis of nanoparticle-label nanocomposite. (A) The optical density of Au-embedded nanobeads increases with particle size and schematic illustration of size control of nanobeads loaded with Au labels in a self-assembly process *via* altering surfactant concentrations, the volume ratio of chloroform/water and the power of sonication. Reproduced from ref. 72, with open access from Ivyspring International Publisher. (B) The fluorescence intensity of DMSN-QD nanobeads increases with particle size and SEM images of 4-sized DMSN-QD nanocomposites and DMSNs. Reproduced with permission from ref. 116. Copyright 2021 John Wiley and Sons.

nanocomposite must first reach the test line and then interacts with the pre-immobilised antibodies.[50,170] In a typical sandwich LFIA system labelled with colloidal Au, the diffusion, advection and antibody–antigen reaction of the gold label collectively affect its binding efficiency at the test line (Fig. 14A).[168] Exploring the kinetics of transport and reaction is a pivotal step in LFIA development and is essential for improving the LFIA performance.[17] The kinetics of transport and reaction can be defined by dimensionless numbers, namely the Péclet number (Pe) and Damköhler number (Da).[168,171] Pe describes the ratio of advective flux to diffusive flux, while the Da depicts the relative rates of reaction to diffusion.[168] The theoretical calculation is outlined as follows:[171]

$$\mathrm{Pe} = \frac{\text{Advection rate}}{\text{Diffusion rate}} = \frac{UR}{D_e} \quad (1)$$

where U denotes the convective velocity ($\sim$0.3 mm s^{-1} for CN140 membrane), R (8 μm) signifies the average radius of cylindrical pores from NC membrane, and D_e is the effective diffusivity in the NC membrane. D_e can be calculated by the following formula:

$$D_e = D\phi/\tau^2 \quad (2)$$

In this context, D stands for the diffusivity of label in solution which can be determined using the Stokes–Einstein equation:

$$D = k_B T/6\pi\mu r \quad (3)$$

k_B represents the Boltzmann constant, T is solution temperature, μ is the solution viscosity, and r is the hydraulic radius of the label.[171] ϕ (0.85) is the membrane porosity and τ ($\sim$1) is the tortuosity of the membrane.[172] According to the above equations, Pe increases as the particle size increases. A calculated Pe $\gg$ 1 suggests that advection timescales are significantly shorter than those of diffusion within an LFIA, making diffusion the rate-limiting step in label transport to the test line.

$$\mathrm{Da} = \frac{\text{Reaction rate}}{\text{Diffusion rate}} = \frac{k'_{on} CR}{D_e} \quad (4)$$

Meanwhile, Da can be determined by eqn (4), where k'_{on} is effective forward reaction rate constant, C is surface density of antibodies at the test line.[171] k'_{on} can be scaled as $n{\cdot}k_{on}$, where k_{on} is forward reaction constant for individual antibody–antigen interaction in the NC membrane ($\sim 7.26 \times 10^2$ M^{-1} s^{-1}),[171] and n reflects the effective number of antibodies that bind the test line per label, which can be estimated by dividing the label surface area ($4\pi R^2$) by the IgG docking area (166 nm^2).[171] Based on the above equations, Da increases as the particle size increases. The calculated Da $\ll$ 1 indicates that diffusion timescales are much shorter than those of reaction within an LFIA. Therefore, reaction is the rate-limiting step in the binding of label at the test line.

For colloidal Au labels with size less than 100 nm, Pe $\gg$ 1 and Da $\ll$ 1 indicate that the reaction ultimately restricts the binding of label at the test line (Fig. 14A). Considering that the small-size Au labels (size $\leq$100 nm) do not settle before

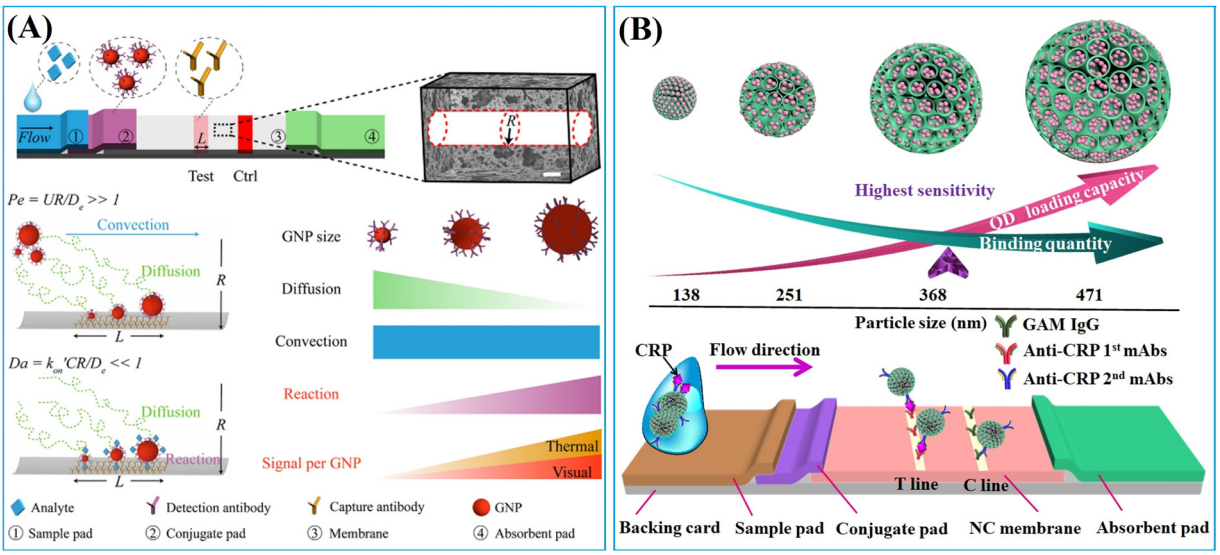

Fig. 14 (A) Architecture of LFIA, assuming that the NC membrane is conceptually simplified as bundles of cylindrical pores with radius R; scale bar is 5 μm. Pe is the ratio of diffusion time to convection time of a colloidal Au label, where Pe $\gg$ 1 in LFIA implies the transport of the colloidal Au label to the test line is diffusion-limited, and Da is the ratio of reaction flux to diffusion flux, where Da $\ll$ 1 in LFIA implies the capture of the colloidal Au label at the test line is reaction-limited. Reprinted with permission from ref. 171. Copyright 2017 American Chemical Society. (B) The QD loading capacity and binding quantity of DMSN-QD as a function of their particle size, and the scheme of DMSN-QD-based LFIA test strip for the detection of CRP. Reprinted with permission from ref. 116. Copyright 2021 John Wiley and Sons.

reaching the test line, a larger Au label can improve the binding efficiency due to increased $n{\cdot}k_{on}$ associated with a larger surface area.[171] When maintaining the same label concentration at various sizes, the binding quantity of a larger size label at the test line increases. In this context, the increase in particle size (size $\leq$100 nm) simultaneously heightens the signal intensity and the binding quantity of the label at the test line, thereby improving the detection performance of LFIA.[171]

In contrast, the nanoparticle-label composite typically has a size exceeding 100 nm, prompting a re-evaluation of the correlation between the binding quantity and the particle size.[72,116,166] The particle size increment may lead to a transition of Da($k'_{on}CR/D_e$) to over 1 at a certain point as k'_{on} enlarges and D_e diminishes with increasing particle size, shifting the rate-limiting step of nanocomposite binding from reaction to diffusion. In cases where Da $\gg$ 1, further enlarging nanocomposite size decreases its binding efficiency due to slower diffusion (Fig. 14B). According to the colloid filtration theory,[173] the binding efficiency influenced by diffusion (η_B) can be determined as $0.487As^{1/3}Pe^{-0.552}$. As depends on membrane porosity:

$$As = 2(1 - \gamma^5)/(2 - 3\gamma + 3\gamma^5 - 2\gamma^6) \quad (5)$$

where $\gamma = (1 - \phi)^{1/3}$. In addition, increased n for large nanocomposite (*e.g.* 400 nm) elevates the risk of non-specific interactions between antibodies on nanocomposite surface and pre-immobilised antibodies on the LFIA membrane, potentially causing false positives.[72,116,166] Thus, decreasing the concentration of large nanocomposite is essential to mitigate false positives. In this context, the binding quantity of larger size nanocomposite at the test line decreases as both the binding efficiency and concentration decrease with growing particle size. Consequently, the ultimate LFIA performance hinges on the signal intensity and binding quantity of nanocomposites at test line, with contrasting tendencies relative to particle size (Fig. 14B). The optimal LFIA performance is achieved by utilizing a medium-sized nanocomposite with a balanced signal intensity and binding quantity.[72,116,166]

1.2.2. Surface chemistry-controlled signal amplification strategies in LFIA. To effectively develop the LFIA platform for detecting low-concentration biomarkers, it is essential that the nanocomposite possess high signal intensity, excellent water dispersibility and strong interaction efficiency and specificity.[115,117,167] In this regard, the surface chemistry of the nanoparticles must be meticulously engineered to meet these criteria and accurately indicate biomolecular recognition events with high precision and a low LoD.[174,175] This section reviews the key role of surface chemistry of nanoparticles in LFIA optimization.

1.2.2.1. The impact on signal intensity. The signal intensity of a nanoparticle-label composite depends on the loading capacity of the nanoparticles and the preservation of label signals. As discussed above, labels can be enriched to nanoparticles through physical adsorption or chemical adsorption. Physical adsorption is primarily driven by hydrophobic–hydrophobic interactions,[57,58,61] and electrostatic attractions.[46,94] Hydrophobic–hydrophobic interactions predominantly occur between the alkyl chains (*e.g.* oleylamine,[72] octadecylamine,[66] oleic acid,[69] and trioctylphosphine oxide[58]) of hydrophobic labels such as QDs and Au labels, and the hydrophobic framework of polymeric nanoparticles consisting of amphiphilic molecules or polystyrene. These interactions also occur between the

aromatic functionalities of hydrophobic molecule labels (*e.g.* Nile red,[61] AIEgens,[57,59] Eu(III) chelates,[47] and the hydrophobic polystyrene). For example, polystyrene, with its hydrophobic chains and steric phenyl rings, forms strong interactions with the aromatic phenyl rings of AIEgen, limiting intramolecular movements and enhancing AIEgen fluorescence considerably (Fig. 15A). These hydrophobic interactions take place between the native surface of the nanoparticle and the label, requiring no post-modification of the nanoparticles.

Enzyme adsorption (*e.g.* artificial miniaturized peroxidase[144]) on the surface of AuNPs involves hydrophobic and/or electrostatic interactions. In cases of electrostatic interactions, PEI, a cationic polymer with a high positive charge density, is frequently utilised to coat the surface of nanoparticles (*e.g.* MNPs,[124,125] AuNPs[156] and nonporous silica nanoparticles[46,98]) to enhance label loading efficiency and maintain nanostructure stability in solution. The PEI-mediated layer-by-layer coating strategy can greatly improve loading efficiency (Fig. 15B).[124,142] Furthermore, PEI coating can prevent nanoparticle aggregation.

The nanoparticle-label integration can be achieved through covalent bonding.[80,113,129] The incorporation of labels with vinyl groups[80,83] into polymeric nanoparticles can be achieved through alkene addition polymerization. The surface modification of nanoparticles with amino[129] and thiol groups[176] represents an effective strategy for enhancing label enrichment. Amines can be coupled with carboxyl groups of labels through carbodiimide-mediated EDC condensation,[129–131] while thiols can coordinate with metal labels.[96,111,116,176] Fig. 15C shows amino and thiol commodified DMSNs for QD enrichment and fluorescence preservation. Amino groups contribute to QD fluorescence preservation through amino-based surface passivation, while thiol groups increase the loading capacity of QDs due to the thiol–metal coordination.

Notably, among these strategies, the hydrophobic functionality,[57,59] PEI coating[46,124,125] and thiol modification strategies[96,111,116,176] emerge as the top three surface chemistry methods for the preparation of nanocomposite with high label loading, uniform label distribution and consistent size distribution.

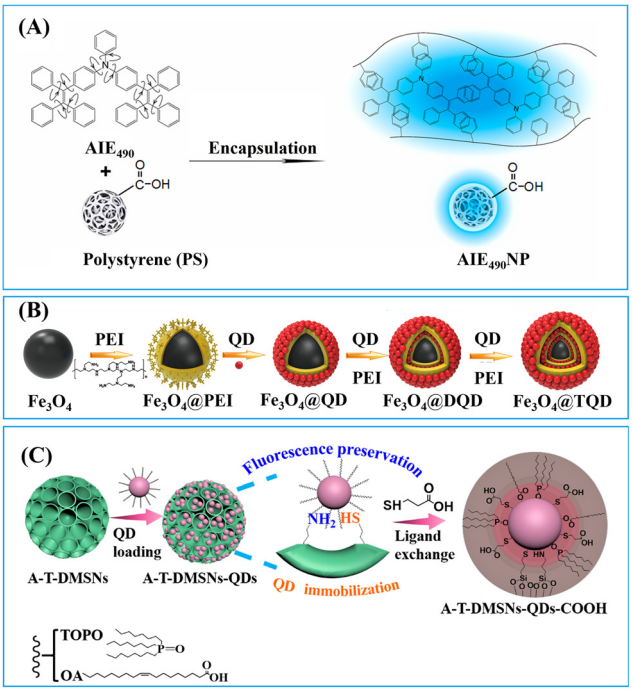

Fig. 15 Surface chemistry of nanoparticles for label enrichment. (A) The hydrophobic–hydrophobic interactions between AIEgens and polystyrene enhance AIEgen fluorescence by restraining intramolecular motions. Reproduced with permission from ref. 57, Copyright 2022 Elsevier. (B) Surface coating of PEI to promote enhanced electrostatic interactions. Reproduced with permission from ref. 124. Copyright 2021 American Chemical Society. (C) Amino- and thiol-modified DMSNs for QD loading and signal preservation. Reproduced with permission from ref. 115. Copyright 2021 American Chemical Society.

1.2.2.2. The impact on binding quantity. The binding quantity of nanocomposite at test line is greatly affected by its water-dispersity. Carboxylation emerges as the most promising strategy to enhance its water-dispersity. Currently, nearly all the commercially available fluorescent polystyrene spheres used in LFIA are carboxyl-modified.[55,177,178] This modification is attributed not only to the ease of conjugating carboxyl group with antibodies through the EDC method,[175] but also to their pK_a of approximately 4,[179] facilitating deprotonation in water and enhancing the nanocomposite dispersibility.[176] Various approaches have been devised to introduce the carboxyl groups onto the outer surface of nanocomposite. For example, the carboxyl groups can be incorporated by using monomers containing carboxyl or acid anhydride functionalities (*e.g.*, acrylic acid,[47,78] methacrylic acid,[80] methyl methacrylate,[82] and maleic anhydride[83]) during the polymerisation process. Additionally, the maleic anhydride in an amphiphilic copolymer like poly (styrene-*co*-maleic anhydride)[69] or polymer PMAO[67,77] that is utilised in the emulsion assembly strategy can also contribute carboxyl groups to nanocomposites. Besides, the saline chemistry enables the facile surface functionalisation of the carboxyl groups. Typically, this involves initially coating a silica shell for the subsequent carboxyl modification. The carboxyl groups can be directly grafted on the silica surface by using 3-triethoxysilylpropyl succinic anhydride,[147,180] or by converting the amino groups into carboxyl groups through reactions with the succinic anhydride[111,176] or polyacrylic acid.[167]

The efficiency and specificity of the antibodies attached to the nanocomposites in recognizing the target analyte affects the amount of binding of the nanocomposites on the test line. The oriented immobilization of the antibodies on the nanocomposite surface played a pivotal role in improving the reaction efficiency and specificity. The accessibility of antigen binding sites (Fab fragment) determines the efficiency of antibody–antigen binding. A nucleophilic addition reaction between the hydrazide group of the nanocomposites and the aldehyde group of the Fc region of the antibodies enables the specific attachment of antibodies to the surface of the nanocomposites (Fig. 16A). Compared to the carbodiimide method,

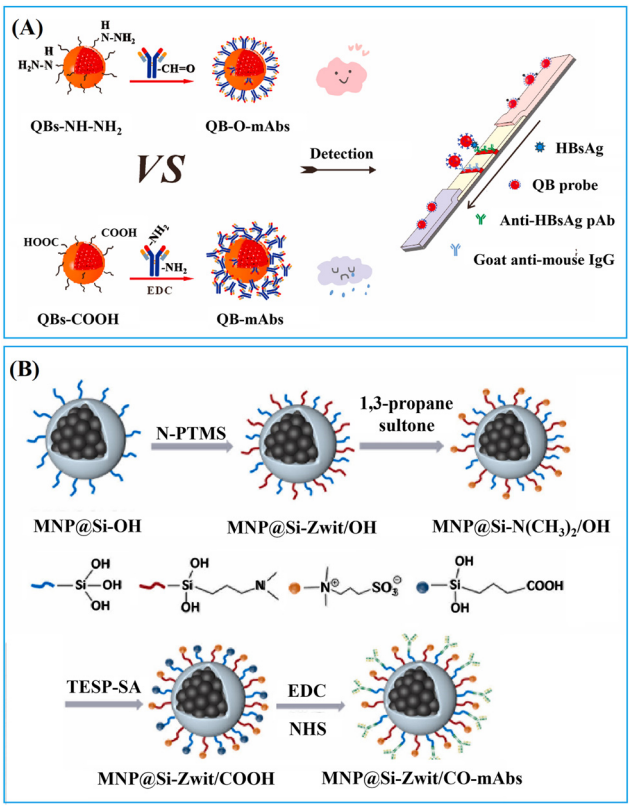

Fig. 16 Strategies for enhancing reaction efficiency and specificity. (A) The hydrazide mediated oriented coupling strategy. Reprinted with permission from ref. 66. Copyright 2021 Elsevier. (B) Utilization of zwitterionic ligands to reduce nonspecific binding. Reproduced with permission from ref. 180. Copyright 2024 Elsevier.

this hydrazide-mediated oriented coupling strategy reduced the LoD by approximately fourfold in the detection of the hepatitis B surface antigen.[66]

Effective surface blocking of antibodies also benefits the reaction efficiency and specificity. The incorporation of zwitterionic ligands, which simultaneously possess positive and negative charges, leading to high hydration capacity and antifouling properties, can further reduce nonspecific binding. Fig. 16B depicts the introduction of zwitterionic groups through a nucleophilic addition reaction using 1,3-propanesultone following the co-hydrolysis of the silica precursor *N*,*N*-diethyl-3-(trimethoxysilyl) propylamine and tetraethyl orthosilicate. The zwitterionic groups effectively prevent nonspecific adhesion. Moreover, antibody-modified nanocomposites are usually blocked with 1–10% (w/v) bovine serum albumin (BSA) to prevent undesired non-specific binding.[58,181] Alternative blocking regents include other protein products (*e.g.* casein[131] and skim milk[68]) and polymers (*e.g.* PEG 20 000[156] and PEG-400[144]). Additionally, quenching reagents such as glycine[109] and ethanolamine,[182] along with Tween-20,[135] are often combined with BSA to enhance blocking performance.

In general, surface chemistry plays a crucial role in determining the binding quantity of nanocomposites by influencing water dispersibility, reaction efficiency and specificity. Carboxylation acts as a fundamental strategy to enhance water dispersibility, while the oriented immobilization of antibodies and effective surface blocking techniques are pivotal in improving reaction efficiency and specificity. The integration of recognition antibodies onto nanocomposites can be achieved through noncovalent or covalent bonding, with the latter providing control over orientation and stability. Furthermore, the introduction zwitterionic ligands and the use of agents to block antibody-modified nanocomposites can effectively reduce nonspecific binding.

2. Conclusion and perspectives

The utilization of nanocomposites for signal amplification in LFIA detection systems represents a significant advancement in the field of modern biosensing. Nanocomposites possess unique optical, electronic, catalytic, and magnetic properties that can markedly enhance detection sensitivity and specificity. This review delves into the engineering of nanoparticles for LFIA signal amplification, emphasizing the importance of comprehensively understanding the relationship between the physicochemical properties of nanoparticles and their performance in LFIA applications. The advantages and potentials of these nanoparticle-assisted strategies in LFIA can be summarized into five aspects: (1) high sensitivity: nanocomposites amplify detection signals, enabling the identification of analytes at lower concentrations. (2) Multifunctionality: certain nanoparticles can be employed for both signal amplification and target pre-concentration. (3) Diverse signal outputs: nanocomposites offer various signal outputs, such as optical, and electrochemical signals, and (4) quantitative detection: through integration with digital health technologies, highly sensitive nanoparticle assisted LFIA can offer more precise quantitative analyses, whereas traditional lateral flow strips only provide qualitative or semi-quantitative results.

Despite the numerous advantages of nanoscale signal amplification technologies, its application continues to encounter various limitations and challenges to be urgently addressed, including the following.

2.1. Balancing sensitivity and specificity

While enhancing sensitivity, precautions must be taken to avoid increasing the risk of false positives.

2.2. Stability

Nanocomposites may aggregate or degrade over time due to prolonged storage or extreme environmental conditions, affecting their functionality. Therefore, there is a need to develop more stable nanocomposites and optimize storage conditions.

2.3. Batch consistency

Maintaining high reproducibility and consistency in the preparation of nanocomposites is crucial to ensure the accuracy of detection results.

2.4. Ease of operation

The use of nanocomposites should not overly complicate the detection process, as it could impact the user-friendliness of LFIA detection systems.

2.5. Cost-effectiveness

Nanocomposites may elevate testing costs, necessitating the development of cost-efficient synthetic methods.

With the development of new materials and technologies, it is believed that addressing these limitations and fully harnessing the advantages of nanocomposites could lead the LFIA to achieve greater breakthroughs in sensitivity, stability, and applicability in the future.

Author contributions

FG and ZG conceptualized and wrote the manuscript. SY created the schemes and figures. LH provided oversight and made essential revisions. All authors reviewed and endorsed the final version of the manuscript.

Conflicts of interest

There are no conflicts to declare.

Acknowledgements

This work was supported by the National Natural Science Foundation of China (Grant no. 82372148) and the National Key Research and Development Program of China (no. 2021YFF0703500 and 2022YFE0103500).

References

1 J. Budd, B. S. Miller, N. E. Weckman, D. Cherkaoui, D. Huang, A. T. Decruz, N. Fongwen, G. Han, M. Broto, C. S. Estcourt, J. Gibbs, D. Pillay, P. Sonnenberg, R. Meurant, M. R. Thomas, N. Keegan, M. M. Stevens, E. Nastouli, E. J. Topol, A. M. Johnson, M. Shahmanesh, A. Ozcan, J. J. Collins, M. F. Suarez, B. Rodriguez, R. W. Peeling and R. A. McKendry, *Nat. Rev. Bioeng.*, 2023, **1**, 13–31.
2 M. Naseri, Z. M. Ziora, G. P. Simon and W. Batchelor, *Rev. Med. Virol.*, 2022, **32**, e2263.
3 P. Sadeghi, H. Sohrabi, M. Hejazi, A. Jahanban-Esfahlan, B. Baradaran, M. Tohidast, M. R. Majidi, A. Mokhtarzadeh, S. M. Tavangar and M. de la Guardia, *Trends Anal. Chem.*, 2021, **145**, 116460.
4 C. Zheng, K. Wang, W. Zheng, Y. Cheng, T. Li, B. Cao, Q. Jin and D. Cui, *Analyst*, 2021, **146**, 1514.
5 L. Khelifa, Y. Hu, N. Jiang and A. K. Yetisen, *Lab Chip*, 2022, **22**, 2451–2475.
6 F. Mazur, A. D. Tjandra, Y. Zhou, Y. Gao and R. Chandrawati, *Nat. Rev. Bioeng.*, 2023, **1**, 180–192.
7 H. Sohrabi, M. R. Majidi, P. Khaki, A. Jahanban-Esfahlan, M. de la Guardia and A. Mokhtarzadeh, *Compr. Rev. Food Sci. Food Saf.*, 2022, **21**, 1868–1912.
8 Q. Zhang, L. Fang, B. Jia, N. Long, L. Shi, L. Zhou, H. Zhao and W. Kong, *Trends Anal. Chem.*, 2021, **144**, 116427.
9 Z. Farka, J. C. Brandmeier, M. J. Mickert, M. Pastucha, K. Lacina, P. Skládal, T. Soukka and H. H. Gorris, *Adv. Mater.*, 2024, **36**, 2307653.
10 Y. Zhou, Y. Wu, L. Ding, X. Huang and Y. Xiong, *Trends Anal. Chem.*, 2021, **145**, 116452.
11 J. Dinnes, P. Sharma, S. Berhane, S. S. van Wyk, N. Nyaaba, J. Domen, M. Taylor, J. Cunningham, C. Davenport, S. Dittrich, D. Emperador, L. Hooft, M. M. G. Leeflang, M. D. F. McInnes, R. Spijker, J. Y. Verbakel, Y. Takwoingi, S. Taylor-Phillips, A. Van den Bruel and J. J. Deeks, *Cochrane Database Syst. Rev.*, 2022, (7), CD013705.
12 E. Valera, A. Jankelow, J. Lim, V. Kindratenko, A. Ganguli, K. White, J. Kumar and R. Bashir, *ACS Nano*, 2021, **15**, 7899–7906.
13 M. Cretich, G. G. Daaboul, L. Sola, M. S. Ünlü and M. Chiari, *Trends Biotechnol.*, 2015, **33**, 343–351.
14 S. O. Kelley, *ACS Sens.*, 2017, **2**, 193–197.
15 P. R. Srinivas, B. S. Kramer and S. Srivastava, *Lancet Oncol.*, 2001, **2**, 698–704.
16 J. Castillo-León, R. Trebbien, J. J. Castillo and W. E. Svendsen, *Analyst*, 2021, **146**, 3750–3776.
17 Y. Liu, L. Zhan, Z. Qin, J. Sackrison and J. C. Bischof, *ACS Nano*, 2021, **15**, 3593–3611.
18 L. Roy, P. Buragohain and V. Borse, *Biosens. Bioelectron. X*, 2022, **10**, 100098.
19 H. R. Boehringer and B. J. O'farrell, *Clin. Chem.*, 2022, **68**, 52–58.
20 A. C. Mirica, D. Stan, I. C. Chelcea, C. M. Mihailescu, A. Ofiteru and L. A. Bocancia-Mateescu, *Front. Bioeng. Biotechnol.*, 2022, **10**, 922772.
21 Y. Deng, H. Jiang, X. Li and X. Lv, *Microchim. Acta*, 2021, **188**, 379.
22 J. D. Bishop, H. V. Hsieh, D. J. Gasperino and B. H. Weigl, *Lab Chip*, 2019, **19**, 2486–2499.
23 S. Gao, L. Niu, R. Zhou, C. Wang, X. Zheng, D. Zhang, X. Huang, Z. Guo and X. Zou, *Int. J. Biol. Macromol.*, 2024, **257**, 128621.
24 A. K. Trilling, J. Beekwilder and H. Zuilhof, *Analyst*, 2013, **138**, 1619–1627.
25 L. F. Yang, M. Ling, N. Kacherovsky and S. H. Pun, *Chem. Sci.*, 2023, **14**, 4961.
26 T. Wang, L. Chen, A. Chikkanna, S. Chen, I. Brusius, N. Sbuh and R. N. Veedu, *Theranostics*, 2021, **11**, 5174–5196.
27 A. N. Baker, G. W. Hawker-Bond, P. G. Georgiou, S. Dedola, R. A. Field and M. I. Gibson, *Chem. Soc. Rev.*, 2022, **51**, 7238–7259.
28 L. Zhang, H. Jiang, Z. Zhu, J. Liu and B. Li, *Talanta*, 2022, **243**, 123388.
29 M. M. Kaminski, O. O. Abudayyeh, J. S. Gootenberg, F. Zhang and J. J. Collins, *Nat. Biomed. Eng.*, 2021, **5**, 643–656.

30 Y. Tang, L. Gao, W. Feng, C. Guo, Q. Yang, F. Li and X. C. Le, *Chem. Soc. Rev.*, 2021, **50**, 11844–11869.
31 S. Modha, C. Castro and H. Tsutsui, *Biosens. Bioelectron.*, 2021, **178**, 113026.
32 J. Park, *Sensors*, 2022, **22**, 7398.
33 Z. Wang, J. Zhao, X. Xu, L. Guo, L. Xu, M. Sun, S. Hu, H. Kuang, C. Xu and A. Li, *Small Methods*, 2022, **6**, 2101143.
34 Z. Su, W. Dou, X. Liu, J. Ping, D. Li, Y. Ying and L. Xie, *TrAC, Trends Anal. Chem.*, 2022, **154**, 116673.
35 V. T. Nguyen, S. Song, S. Park and C. Joo, *Biosens. Bioelectron.*, 2020, **152**, 112015.
36 X. Chen, L. Ding, X. Huang and Y. Xiong, *Theranostics*, 2022, **12**, 574–602.
37 O. I. Guliy and L. A. Dykman, *Biosens. Bioelectron. X*, 2024, **17**, 100457.
38 L. Wang, X. Wang, L. Cheng, S. Ding, G. Wang, J. Choo and L. Chen, *Biosens. Bioelectron.*, 2021, **189**, 113360.
39 K. Kim, L. Kashefi-Kheyrabadi, Y. Joung, K. Kim, H. Dang, S. G. Chavan, M. H. Lee and J. Choo, *Sens. Actuators, B*, 2021, **329**, 129214.
40 B. Fang, Q. Xiong, H. Duan, Y. Xiong and W. Lai, *Trends Anal. Chem.*, 2022, **157**, 116754.
41 W. He, M. Wang, P. Cheng, Y. Liu and M. You, *Trends Anal. Chem.*, 2024, **173**, 117641.
42 D. Calabria, M. M. Calabretta, M. Zangheri, E. Marchegiani, I. Trozzi, M. Guardigli, E. Michelini, F. Di Nardo, L. Anfossi, C. Baggiani and M. Mirasoli, *Sensors*, 2021, **21**, 1–19.
43 J. Cheng, G. Yang, J. Guo, S. Liu and J. Guo, *Analyst*, 2022, **147**, 554–570.
44 I. Y. Goryacheva, E. S. Speranskaya, V. V. Goftman, D. Tang and S. De Saeger, *Trends Anal. Chem.*, 2015, **66**, 53–62.
45 O. S. Wolfbeis, *Angew. Chem., Int. Ed.*, 2013, **52**, 9864–9865.
46 X. Yang, X. Cheng, H. Wei, Z. Tu, Z. Rong, C. Wang and S. Wang, *J. Nanobiotechnol.*, 2023, **21**, 450.
47 M. Xu, J. Liu, X. Su, Q. Zhou, H. Yuan, Y. Wen, Y. Cheng and F. Li, *Sci. China: Chem.*, 2021, **64**, 2125–2133.
48 R. Chen, X. Chen, Y. Zhou, T. Lin, Y. Leng, X. Huang and Y. Xiong, *ACS Nano*, 2022, **16**, 3351–3361.
49 Y. Wu, R. D. Tilley and J. Justin Gooding, *J. Am. Chem. Soc.*, 2019, **141**, 1162–1170.
50 E. B. Bahadır and M. K. Sezgintürk, *Trends Anal. Chem.*, 2016, **82**, 286–306.
51 M. Millipore, *Rapid lateral flow test strips: considerations for product development*, Billerica, MA, Germany, 2013.
52 M. A. Mansfield, *Lateral Flow Immunoassay*, Humana Press, 2009, pp. 1–19.
53 R. Krska and A. Molinelli, *Anal. Bioanal. Chem.*, 2008, **393**, 67–71.
54 F. Hou, S. Sun, S. W. Abdullah, Y. Tang, X. Li and H. Guo, *Anal. Methods*, 2023, **15**, 2154–2180.
55 R. Hu, T. Liao, Y. Ren, W. Liu, R. Ma, X. Wang, Q. Lin, G. Wang and Y. Liang, *Nano Res.*, 2022, **15**, 7313–7319.
56 D. Wang, S. He, X. Wang, Y. Yan, J. Liu, S. Wu, S. Liu, Y. Lei, M. Chen, L. Li, J. Zhang, L. Zhang, X. Hu, X. Zheng, J. Bai, Y. Zhang, Y. Zhang, M. Song and Y. Tang, *Nat. Biomed. Eng.*, 2020, **4**, 1150–1158.
57 L. Bian, Z. Li, A. He, B. Wu, H. Yang, Y. Wu, F. Hu, G. Lin and D. Zhang, *Biomaterials*, 2022, **288**, 121694.
58 J. Hou, Y. Cao, Q. Deng, Q. Zhang, X. Deng, Z. Chen and Z. Zhong, *Anal. Chim. Acta*, 2024, **1288**, 342143.
59 R. Chen, C. Ren, M. Liu, X. Ge, M. Qu, X. Zhou, M. Liang, Y. Liu and F. Li, *ACS Nano*, 2021, **15**, 8996–9004.
60 H. Li, B. Dong, L. Dou, W. Yu, X. Yu, K. Wen, Y. Ke, J. Shen and Z. Wang, *Sens. Actuators, B*, 2020, **324**, 128771.
61 Y. Cai, K. Kang, Y. Liu, Y. Wang and X. He, *Anal. Biochem.*, 2018, **556**, 129–135.
62 R. Chen, X. Zhou, Y. Wu, Q. Liu, Q. Liu, J. Huang and F. Li, *Sens. Actuators, B*, 2021, **328**, 129050.
63 C. Li, Z. Zou, H. Liu, Y. Jin, G. Li, C. Yuan, Z. Xiao and M. Jin, *Talanta*, 2021, **225**, 122064.
64 J. Xia, Y. Liu, M. Ran, W. Lu, L. Bi, Q. Wang, D. Lu and X. Cao, *RSC Adv.*, 2020, **10**, 29156–29170.
65 Y. Matsumura, Y. Enomoto, M. Takahashi and S. Maenosono, *ACS Appl. Mater. Interfaces*, 2018, **10**, 31977–31987.
66 J. Hu, S. Zhou, L. Zeng, Q. Chen, H. Duan, X. Chen, X. Li and Y. Xiong, *Talanta*, 2021, **223**, 121723.
67 G. Chen, X. Chen, G. Xu, X. Wei, X. Lin, Y. Su, Y. Xiong and X. Huang, *Food Chem.*, 2023, **412**, 135580.
68 Y. Li, X. Chen, J. Yuan, Y. Leng, W. Lai, X. Huang and Y. Xiong, *J. Dairy Sci.*, 2020, **103**, 6940–6949.
69 C. Zhou, X. Yang, C. Zhang, S. Zhang and P. Zhang, *Surf. Interfaces*, 2021, **24**, 101057.
70 X. Chen, X. Miao, T. Ma, Y. Leng, L. Hao, H. Duan, J. Yuan, Y. Li, X. Huang and Y. Xiong, *Foods*, 2021, **10**, 1488.
71 Y. Zhou, Y. Chen, W. Liu, H. Fang, X. Li, L. Hou, Y. Liu, W. Lai, X. Huang and Y. Xiong, *Sens. Actuators, B*, 2021, **343**, 130139.
72 X. Chen, Y. Leng, L. Hao, H. Duan, J. Yuan, W. Zhang, X. Huang and Y. Xiong, *Theranostics*, 2020, **10**, 3737.
73 B. Liu, P. Li, Y. Wang, Y. Guo, H. Zhang, S. Dong, Y. Xiong and C. Zhang, *Food Anal. Methods*, 2020, **13**, 1736–1745.
74 G. Zhang, S. Xu, Y. Xiong, H. Duan, W. Chen, X. Li, M. Yuan and W. Lai, *Biosens. Bioelectron.*, 2019, **135**, 173–180.
75 L. Hao, Y. Leng, L. Zeng, X. Chen, J. Chen, H. Duan, X. Huang, Y. Xiong and X. Chen, *Adv. Sci.*, 2020, **7**, 1902433.
76 L. Hao, J. Chen, X. Chen, T. Ma, X. Cai, H. Duan, Y. Leng, X. Huang and Y. Xiong, *Food Chem.*, 2021, **336**, 127710.
77 Y. Su, X. Chen, H. Huang, Y. Wu, X. Shen, X. Lin, K. Sun, X. Fan, X. Huang and Y. Xiong, *Aggregate*, 2023, e459.
78 Z. Li, Q. Liu, Y. Li, W. Yuan and F. Y. Li, *J. Rare Earths*, 2021, **39**, 11–18.
79 Z. Chen, Z. Zhang, X. Zhai, Y. Li, L. Lin, H. Zhao, L. Bian, P. Li, L. Yu, Y. Wu and G. Lin, *Anal. Chem.*, 2020, **92**, 7226–7231.
80 Q. Xu, Y. Wang, P. Gao and Y. Jiang, *New J. Chem.*, 2021, **45**, 10618–10625.
81 C. Zhou, T. Liu, X. Yang, C. Zhang, S. Zhang and P. Zhang, *Opt. Mater.*, 2020, **99**, 109582.
82 F. Shi, Y. Tang, Z. H. Xu, Y. X. Sun, M. Z. Ma and C. F. Chen, *J. Appl. Microbiol.*, 2021, **00**, 1–10.

83 G. Wang, L. Yang, C. Li, H. Yu, Z. He, C. Yang, J. Sun, P. Zhang, X. Gu and B. Tang, *Mater. Chem. Front.*, 2021, **5**, 2452–2458.
84 S. Zhou, Y. Peng, J. Hu, H. Duan, T. Ma, L. Hou, X. Li and Y. Xiong, *Microchem. J.*, 2020, **159**, 105533.
85 X. Lai, X. Lv, G. Zhang, Z. Xiong, W. Lai and J. Peng, *Food Anal. Methods*, 2020, **13**, 2258–2268.
86 C. Hofmann, A. Duerkop and A. J. Baeumner, *Angew. Chem., Int. Ed.*, 2019, **58**, 12840–12860.
87 S. Chatterjee, X.-S. Li, F. Liang and Y.-W. Yang, *Small*, 2019, **15**, 1904569.
88 J. Wang, Q. Ma, Y. Wang, Z. Li, Z. Li and Q. Yuan, *Chem. Soc. Rev.*, 2018, **47**, 8766–8803.
89 W. Wei, M. Wei and S. Liu, *Rev. Anal. Chem*, 2012, **31**, 163–176.
90 H. Jung, S. H. Park, J. Lee, B. Lee, J. Park, Y. Seok, J. H. Choi, M. G. Kim, C. S. Song and J. Lee, *Anal. Chem.*, 2020, **93**, 792–800.
91 Y. Zhu, L. Ao, S. Chu, Y. Liao, J. Wang, J. Hu and L. Huang, *Adv. Funct. Mater.*, 2024, **2316147**, 1–13.
92 B. Zhang, X. Yang, X. Liu, J. Li, C. Wang and S. Wang, *RSC Adv.*, 2020, **10**, 2483–2489.
93 X. Yang, X. Liu, B. Gu, H. Liu, R. Xiao, C. Wang and S. Wang, *Microchim. Acta*, 2020, **187**, 1–11.
94 T. Dong, R. Yin, Q. Yu, W. Qiu, K. Li, L. Qian, H. Li, B. Shen and G. Liu, *Anal. Chim. Acta*, 2021, **1147**, 56–63.
95 S. K. Kim, H. Sung, S. H. Hwang and M. N. Kim, *Biochip. J.*, 2022, **16**, 175–182.
96 S. Bock, H. M. Kim, J. Kim, J. An, Y. S. Choi, X. H. Pham, A. Jo, K. M. Ham, H. Song, J. W. Kim, E. Hahm, W. Y. Rho, S. H. Lee, S. M. Park, S. Lee, D. H. Jeong, H. Y. Lee and B. H. Jun, *Nanomaterials*, 2022, **12**, 1–11.
97 H. M. Kim, C. Oh, J. An, S. Baek, S. Bock, J. Kim, H. S. Jung, H. Song, J. W. Kim, A. Jo, D. E. Kim, W. Y. Rho, J. Y. Jang, G. J. Cheon, H. J. Im and B. H. Jun, *Nanomaterials*, 2021, **11**, 1–10.
98 J. Zhao, H. Han, Z. Liu, J. Chen, X. Liu, Y. Sun, B. Wang, B. Zhao, Y. Pang and R. Xiao, *Anal. Chim. Acta*, 2024, **1295**, 342306.
99 C. Wang, X. Yang, S. Zheng, X. Cheng, R. Xiao, Q. Li, W. Wang, X. Liu and S. Wang, *Sens. Actuators, B*, 2021, **345**, 130372.
100 S. Zheng, X. Yang, B. Zhang, S. Cheng, H. Han, Q. Jin, C. Wang and R. Xiao, *Food Chem.*, 2021, **363**, 130400.
101 C. Wang, X. Yang, B. Gu, H. Liu, Z. Zhou, L. Shi, X. Cheng and S. Wang, *Anal. Chem.*, 2020, **92**, 15542–15549.
102 C. Wang, D. Shi, N. Wan, X. Yang, H. Liu, H. Gao, M. Zhang, Z. Bai, D. Li, E. Dai, Z. Rong and S. Wang, *Analyst*, 2021, **146**, 3908–3917.
103 Z. Su, G. Zhao and W. Dou, *Anal. Methods*, 2021, **13**, 2313–2319.
104 D. Hong, E.-J. Jo, K. Kim, M.-B. Song and M.-G. Kim, *Small*, 2020, **16**, 2004535.
105 X. Jia, K. Wang, X. Li, Z. Liu, Y. Liu, R. Xiao and S. Wang, *Nanomed. Nanotechnol., Biol. Med.*, 2022, **41**, 102522.
106 L. Shi, L. Xu, R. Xiao, Z. Zhou, C. Wang, S. Wang and B. Gu, *Front. Microbiol.*, 2020, **11**, 596005.
107 V. G. Grigorenko, I. P. Andreeva, G. V. Presnova, D. E. Presnov, E. A. Yakovleva and A. P. Osipov, *Moscow Univ. Chem. Bull.*, 2020, **75**, 207–212.
108 H. M. Kim, J. Kim, S. Bock, J. An, Y. S. Choi, X. H. Pham, M. G. Cha, B. Seong, W. Kim, Y. H. Kim, H. Song, J. W. Kim, S. min Park, S. H. Lee, W. Y. Rho, S. Lee, D. H. Jeong, H. Y. Lee and B. H. Jun, *Sensors*, 2021, **21**, 4099.
109 R. Narayan, U. Y. Nayak, A. M. Raichur and S. Garg, *Pharmaceutics*, 2018, **10**, 118.
110 C. Xu, C. Lei, Y. Wang and C. Yu, *Angew. Chem., Int. Ed.*, 2022, **61**, e202112752.
111 L. Ao, T. Liao, L. Huang, S. Lin, K. Xu, J. Ma, S. Qiu, X. Wang and Q. Zhang, *Chem. Eng. J.*, 2022, **436**, 135204.
112 F. Gao, C. Liu, Y. Yao, C. Lei, S. Li, L. Yuan, H. Song, Y. Yang, J. Wan and C. Yu, *Biosens. Bioelectron.*, 2022, **199**, 113892.
113 Y. Wang, C. Deng, S. Qian, H. Li, P. Fu, H. Zhou and J. Zheng, *Food Chem.*, 2023, **399**, 133970.
114 S. Tadepalli, Z. Wang, K. K. Liu, Q. Jiang, J. Slocik, R. R. Naik and S. Singamaneni, *Langmuir*, 2017, **33**, 6611–6619.
115 F. Gao, C. Lei, Y. Liu, H. Song, Y. Kong, J. Wan and C. Yu, *ACS Appl. Mater. Interfaces*, 2021, **13**, 21507–21515.
116 F. Gao, Y. Liu, C. Lei, C. Liu, H. Song, Z. Gu, P. Jiang, S. Jing, J. Wan and C. Yu, *Small Methods*, 2021, **5**, 2000924.
117 D. Li, M. Huang, Z. Shi, L. Huang, J. Jin, C. Jiang, W. Yu, Z. Guo and J. Wang, *Anal. Chem.*, 2022, **94**, 2996–3004.
118 L.-D. Xu, F.-L. Du, J. Zhu and S.-N. Ding, *Analyst*, 2021, **146**, 706–713.
119 L. Di Xu, J. Zhu and S. N. Ding, *Analyst*, 2021, **146**, 5055–5060.
120 L. Huang, J. Jin, L. Ao, C. Jiang, Y. Zhang, H.-M. Wen, J. Wang, H. Wang and J. Hu, *ACS Appl. Mater. Interfaces*, 2020, **12**, 58149–58160.
121 J. Yuan, L. Wang, L. Huang, K. He, H. Wang, X. Xu, B. Su and J. Wang, *Anal. Chem.*, 2024, **96**, 220–228.
122 J. Wang, C. Jiang, J. Jin, L. Huang, W. Yu, B. Su and J. Hu, *Angew. Chem., Int. Ed.*, 2021, **60**, 13042–13049.
123 L. Huang, Y. Zhang, T. Liao, K. Xu, C. Jiang, D. Zhuo, Y. Wang, H. Wen, J. Wang, L. Ao and J. Hu, *Small*, 2021, **17**, 2100862.
124 C. Wang, X. Cheng, L. Liu, X. Zhang, X. Yang, S. Zheng, Z. Rong and S. Wang, *ACS Appl. Mater. Interfaces*, 2021, **13**, 40342–40353.
125 J. Tu, T. Wu, Q. Yu, J. Li, S. Zheng, K. Qi, G. Sun, R. Xiao and C. Wang, *J. Hazard. Mater.*, 2023, **448**, 130912.
126 C. Wang, C. Wang, X. Wang, K. Wang, Y. Zhu, Z. Rong, W. Wang, R. Xiao and S. Wang, *ACS Appl. Mater. Interfaces*, 2019, **11**, 19495–19505.
127 L. Dou, Y. Bai, M. Liu, S. Shao, H. Yang, X. Yu, K. Wen, Z. Wang, J. Shen and W. Yu, *Biosens. Bioelectron.*, 2022, **204**, 114093.
128 X. Liu, K. Wang, B. Cao, L. Shen, X. Ke, D. Cui, C. Zhong and W. Li, *Anal. Chem.*, 2021, **93**, 3626–3634.
129 F. Wang, X. Li, Z. Liu, X. Zhao, C. Zhao, G. Hou, Q. Liu and X. Liu, *Anal. Chem.*, 2024, **96**, 2059–2067.

130 Z. Huang, Z. Xiong, Y. Chen, S. Hu and W. Lai, *J. Agric. Food Chem.*, 2019, **67**, 3028–3036.
131 Z. Huang, J. Peng, J. Han, G. Zhang, Y. Huang, M. Duan, D. Liu, Y. Xiong, S. Xia and W. Lai, *Food Chem.*, 2019, **276**, 333–341.
132 J. Wang, C. Jiang, J. Yuan, L. Tong, Y. Wang, D. Zhuo, L. Huang, W. Ni, J. Zhang, M. Huang, D. Li, B. Su and J. Hu, *Anal. Chem.*, 2022, **94**, 10865–10873.
133 Z. Bai, H. Wei, X. Yang, Y. Zhu, Y. Peng, J. Yang, C. Wang, Z. Rong and S. Wang, *Sens. Actuators, B*, 2020, **325**, 128780.
134 L. Gloag, M. Mehdipour, D. Chen, R. D. Tilley and J. J. Gooding, *Adv. Mater.*, 2019, **31**, 1904385.
135 M. S. Kim, S. H. Kweon, S. Cho, S. S. A. An, M. Il Kim, J. Doh and J. Lee, *ACS Appl. Mater. Interfaces*, 2017, **9**, 35133–35140.
136 Z. Xie, S. Feng, F. Pei, M. Xia, Q. Hao, B. Liu, Z. Tong, J. Wang, W. Lei and X. Mu, *Anal. Chim. Acta*, 2022, **1233**, 340486.
137 W. Shen, C. Wang, X. Yang, C. Wang, Z. Zhou, X. Liu, R. Xiao, B. Gu and S. Wang, *J. Mater. Chem. C*, 2020, **8**, 12854–12864.
138 X. Liu, X. Yang, K. Li, H. Liu, R. Xiao, W. Wang, C. Wang and S. Wang, *Sens. Actuators, B*, 2020, **320**, 128350.
139 S. Liu, L. Dou, X. Yao, W. Zhang, M. Zhao, X. Yin, J. Sun, D. Zhang and J. Wang, *Biosens. Bioelectron.*, 2020, **169**, 112610.
140 T. Zhang, L. Lei, M. Tian, J. Ren, Z. Lu, Y. Liu and Y. Liu, *Talanta*, 2021, **222**, 121478.
141 M. Zhang, M. Li, Y. Zhao, N. Xu, L. Peng, Y. Wang and X. Wei, *Food Res. Int.*, 2021, **142**, 110102.
142 C. Wang, W. Shen, Z. Rong, X. Liu, B. Gu, R. Xiao and S. Wang, *Nanoscale*, 2020, **12**, 795–807.
143 G.-R. Han, H. Ki and M.-G. Kim, *ACS Appl. Mater. Interfaces*, 2020, **12**, 1885–1894.
144 E. Renzi, A. Piper, F. Nastri, A. Merkoçi and A. Lombardi, *Small*, 2023, **19**, 2207949.
145 D. Hong, K. Kim, E.-J. Jo and M.-G. Kim, *Anal. Chem.*, 2021, **93**, 7925–7932.
146 A. J. Qavi, Q. Jiang, M. J. Aman, H. Vu, L. Zetlin, J. M. Dye, J. W. Froude, D. W. Leung, F. Holtsberg, S. L. Crick and G. K. Amarasinghe, *ACS Infect. Dis.*, 2024, **10**, 57–63.
147 D. Hong, E. J. Jo, D. Bang, C. Jung, Y. E. Lee, Y. S. Noh, M. G. Shin and M. G. Kim, *ACS Nano*, 2023, **17**, 16607–16619.
148 M. Song, J. Xing, H. Cai, X. Gao, C. Li, C. Liu, X. Li, X. Fu, S. Ding, W. Cheng and R. Chen, *ACS Nano*, 2023, **17**, 10748–10759.
149 X. Yin, L. Dou, X. Yao, S. Liu, L. Zhang, M. Zhao, L. Su, J. Sun, J. Wang and D. Zhang, *Food Chem.*, 2022, **367**, 130737.
150 J. Zhang, Y. Li, F. Chai, Q. Li, D. Wang, L. Liu, B. Z. Tang and X. Jiang, *Sci. Adv.*, 2022, **8**, eabo1874.
151 K. He, T. Bu, X. Zheng, J. Xia, F. Bai, S. Zhao, X. yu Sun, M. Dong and L. Wang, *J. Hazard. Mater.*, 2022, **425**, 128034.
152 C. Wang, C. Wang, J. Li, Z. Tu, B. Gu and S. Wang, *Biosens. Bioelectron.*, 2022, **214**, 114525.
153 X. Yao, Z. Wang, M. Zhao, S. Liu, L. Su, L. Dou, T. Li, J. Wang and D. Zhang, *Food Chem.*, 2021, **347**, 129001.
154 G. R. Han and M. G. Kim, *Sensors*, 2020, **20**, 2593.
155 J. Deng, M. Yang, J. Wu, W. Zhang and X. Jiang, *Anal. Chem.*, 2018, **90**, 9132–9137.
156 Y. Pan, X. Wei, X. Guo, H. Wang, H. Song, C. Pan and N. Xu, *Biosens. Bioelectron.*, 2021, **194**, 113611.
157 M. Lv, W. Zhou, H. Tavakoli, C. Bautista, J. Xia, Z. Wang and X. J. Li, *Biosens. Bioelectron.*, 2021, **176**, 112947.
158 Y. Zhao, H. Zeng, X.-W. Zhu, W. Lu and D. Li, *Chem. Soc. Rev.*, 2021, **50**, 4484–4513.
159 Y. Wang, Y. Hu, Q. He, J. Yan, H. Xiong, N. Wen, S. Cai, D. Peng, Y. Liu and Z. Liu, *Biosens. Bioelectron.*, 2020, **169**, 112604.
160 Y. S. Wei, M. Zhang, R. Zou and Q. Xu, *Chem. Rev.*, 2020, **120**, 12089–12174.
161 A. Bavykina, N. Kolobov, I. S. Khan, J. A. Bau, A. Ramirez and J. Gascon, *Chem. Rev.*, 2020, **120**, 8468–8535.
162 L. Jiao and H. L. Jiang, *Chem*, 2019, **5**, 786–804.
163 J. Zou, X. Liu, X. Ren, L. Tan, C. Fu, Q. Wu, Z. Huang and X. Meng, *Nanoscale*, 2021, **13**, 7844–7850.
164 J. Yuan, X. Chen, H. Duan, X. Cai, Y. Li, L. Guo, X. Huang and Y. Xiong, *Microchim. Acta*, 2020, **187**, 1–9.
165 X. Cheng, S. Zheng, W. Wang, H. Han, X. Yang, W. Shen, C. Wang and S. Wang, *Chem. Eng. J.*, 2021, **426**, 131836.
166 H. Duan, X. Chen, Y. Wu, Y. Leng, X. Huang and Y. Xiong, *Anal. Chim. Acta*, 2021, **1141**, 136–143.
167 J. Jia, L. Ao, Y. Luo, T. Liao, L. Huang, D. Zhuo, C. Jiang, J. Wang and J. Hu, *Biosens. Bioelectron.*, 2022, **198**, 113810.
168 D. Gasperino, T. Baughman, H. V. Hsieh, D. Bell and B. H. Weigl, *Annu. Rev. Anal. Chem.*, 2018, **11**, 219–244.
169 Y. Yang, J. Tang, H. Song, Y. Yang, Z. Gu, J. Fu, Y. Liu, M. Zhang, Z. Qiao and C. Yu, *Angew. Chem., Int. Ed.*, 2020, **59**, 19610–19617.
170 C. Parolo, A. Sena-Torralba, J. F. Bergua, E. Calucho, C. Fuentes-Chust, L. Hu, L. Rivas, R. Álvarez-Diduk, E. P. Nguyen, S. Cinti, D. Quesada-González and A. Merkoçi, *Nat. Protoc.*, 2020, **15**, 3788–3816.
171 L. Zhan, S. Guo, F. Song, Y. Gong, F. Xu, D. R. Boulware, M. C. McAlpine, W. C. W. Chan and J. C. Bischof, *Nano Lett.*, 2017, **17**, 7207–7212.
172 C. J. Gommes, A.-J. Bons, S. Blacher, J. H. Dunsmuir and A. H. Tsou, *AIChE J.*, 2009, **55**, 2000–2012.
173 G. Boccardo, D. L. Marchisio and R. Sethi, *J. Colloid Interface Sci.*, 2014, **417**, 227–237.
174 S. Zhang, R. Geryak, J. Geldmeier, S. Kim and V. V. Tsukruk, *Chem. Rev.*, 2017, **117**, 12942–13038.
175 K. E. Sapsford, W. R. Algar, L. Berti, K. B. Gemmill, B. J. Casey, E. Oh, M. H. Stewart and I. L. Medintz, *Chem. Rev.*, 2013, **113**, 1904–2074.
176 L. Huang, T. Liao, J. Wang, L. Ao, W. Su and J. Hu, *Adv. Funct. Mater.*, 2018, **28**, 1705380.

177 M. Zhou, X. Chen, X. Shen, X. Lin, P. Chen, Z. Qiao, X. Li, Y. Xiong and X. Huang, *J. Agric. Food Chem.*, 2023, **71**, 4408–4416.
178 X. Wei, X. Chen, Z. Liu, G. Xu, G. Chen, X. Lin, W. Zhan, X. Huang and Y. Xiong, *Anal. Chim. Acta*, 2023, **1247**, 340869.
179 D. D. Perrin, B. Dempsey and E. P. Serjeant, *pKa Prediction for Organic Acids and Bases*, Chapman and Hall, London, 1981.
180 G. Liu, J. Wang, J. Wang, X. Cui, K. Wang, M. Chen, Z. Yang, A. Gao, Y. Shen, Q. Zhang, G. Gao and D. Cui, *Talanta*, 2024, **273**, 125868.
181 Q. Yu, W. Dou, J. Liu, G. Zhao, S. Yang, D. Zhu, Y. Zhao and L. Li, *Anal. Methods*, 2019, **11**, 268–275.
182 J. Li, Y. Lv, N. Li, R. Wu, J. Li, J. You, H. Shen, X. Chen and L. S. Li, *Sens. Actuators, B*, 2021, **344**, 130275.